Efficiency Studies for the GMp Experiment

Barak Schmookler[1], Bashar Aljawrneh[2], and Thir Gautam[3]

[1] *Massachusetts Institute of Technology*
[2] *North Carolina A&T State University*
[3] *Hampton University*

August 19, 2018

Contents

1 Introduction

The GMp experiment [1] seeks to measure the elastic electron-proton cross section at high Q^2. As the first experiment to complete data-taking in Hall A after the *CEBAF* 12 GeV upgrade, GMp is also the first experiment to use some of the new equipment in Hall A. In addition, the GMp experiment's requirement of small uncertainties necessitates a precise determination of detector inefficiencies. In this note, we describe some novel techniques to extract detector efficiencies for the new standard Hall A detectors. Since these detectors will be used in the future, the techniques described here may be useful for upcoming experiments. Note that since GMp is an inclusive measurement, all the efficiencies discussed are for scattered electrons detected in either spectrometer.

Hall A has two spectrometers, the right arm (RHRS) and the left arm (LHRS) [2]. These arms are almost identical in architecture and operation, and they function independently of one another. A picture and schematic of the new RHRS detector stack is shown in figure 1. Particles pass through the detector stack in the direction shown by the arrow in the figure. Each spectrometer contains two scintillator detectors: the S0 scintillator and the S2m scintillator. The S0 scintillator consists of a single paddle with a PMT located at both large and small X values (in the spectrometer transport coordinate system). The S2m scintillator consists of 16 paddles with a PMT a located at both large and small Y values for each paddle. There are three chambers for tracking (the VDC and a straw chamber). Lastly, the gas cherenkov detector and a lead-glass calorimeter are used for particle identification.

In section 2, we discuss the S0 and S2m scintillator efficiencies, as well as the main trigger efficiency. In section 3, we determine the cut efficiencies for the gas cherenkov and calorimeter detectors. We also discuss the removal of background events which show a large signal in the cherenkov detector but no signal in the calorimeter. In section 4, we calculate the so-called one-track

and one-cluster efficiencies for the Vertical Drift Chamber (VDC). In section 5, we discuss how well all the applied cuts suppress cosmic events. Lastly, in section 6 we calculate the computer and electronic live-time for the GMp experiment. We attempt to place reasonable uncertainties on the quantities we extract in each section.

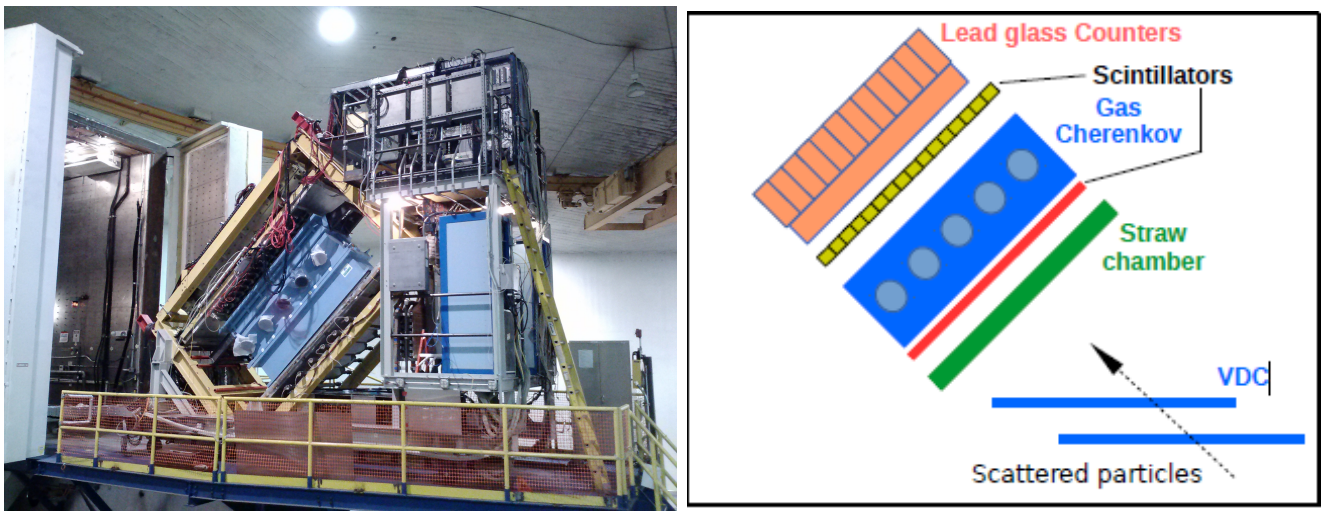

Figure 1: Left: Photo of RHRS detector stack after upgrade (but prior to removal of old S1 detector). Right: Schematic of the RHRS detector stack. The package for the LHRS is similar; however, the calorimeter blocks are arranged differently.

2 Total Scintillator Efficiency

The scintillator efficiency, $\epsilon_{S0(S2m)}$, is defined as $\frac{N_{good}}{N_{total}}$, where N_{total} is a sample of clean electron events with S0 (S2m) not in the trigger and N_{good} is the number of these events that contain above-threshold signals within a wide time window in both PMTs of a S0 (S2m) paddle. (Since the discriminated signals are sent to multi-hit TDCs, only the hit closest to the main timing peak is kept for analysis.) The total scintillator efficiency is defined as the result of $\epsilon_{S0} \times \epsilon_{S2m}$.

For the GMp experiment, the main trigger (T1) was a coincidence of S0 and S2m [3]. So, the evaluation of the scintillator efficiencies is necessary to

determine the main trigger efficiency. In order to accomplish this, two other triggers, T2 and T3, were always enabled. T2 (T3) is a coincidence of S0 (S2m) and the Gas Cherenkov detector, and events of this type can be used to evaluate the efficiency of S2m (S0).

2.1 S0 Scintillator Efficiency (ϵ_{S0})

A T3 event sample is used to evaluate the S0 efficiency. Since the S0 detector is smaller than the T3 detectors and located in front of these detectors, the event sample consists of two categories. In the first category are the events which missed the S0 detector, and they will not be considered for efficiency calculations. In the second category are the events which fell inside the scintillator boundaries and should give signals with large amplitude in both S0 PMTs. The procedure for the S0 scintillator efficiency calculation has the following steps:

- A cut is applied to the particle identification (PID) and tracking detectors to select good electrons. The gas cherenkov vs. calorimeter response is shown in figure 2 for one kinematic setting. The tracking and PID cuts applied here are: one track in the VDC, $N_{pe} > 5$, and $\frac{E}{p} > 0.6(0.7)$ for the LHRS (RHRS).
- As mentioned above, only events that should fire the S0 scintillator are included in the efficiency calculation. To select these events, the track is projected to the S0 detector plane as shown in figure 3. Then only events which project inside the boundary of the detector are included for the efficiency study. (Of course, if the track projection is to be used in this manner, it is necessary for the position of the S0 detector relative to the VDC to be well known [4].) For GMp production data, an additional cut is used to select a clean sample of elastic electrons by a cut on the invariant mass as shown in figure 4.

The S0 efficiency was calculated for every production run. The efficiency was found to be stable within every individual kinematic. In addition, an inelastic run which gave reasonably uniform illumination across the focal plane was used to test the efficiency across the entire S0 detector (i.e. in different bins of the track X and Y projection). As shown in figures 5 and 6,

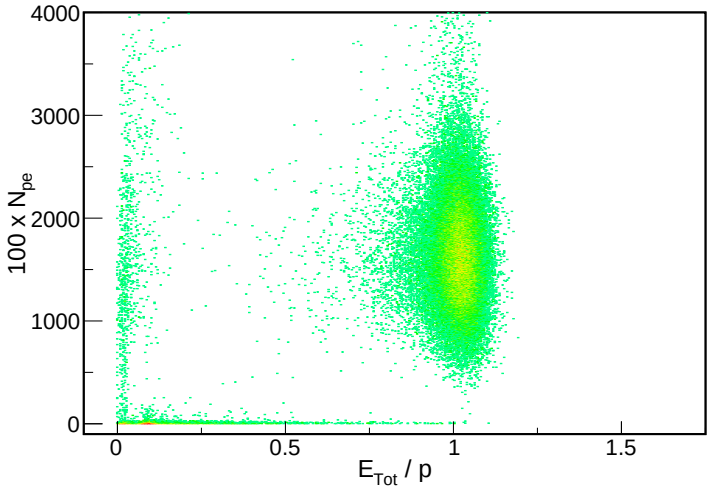

Figure 2: Gas cherenkov vs. total calorimeter response for GMp kinematic k3-6. Good electrons are selected by the cut described in the text.

the efficiency is stable across the entire S0 detector[1]. So, a single efficiency was extracted for each kinematic; these efficiencies are shown in table 1.

2.2 S2m Scintillator Efficiency (ϵ_{S2m})

A T2 event sample is used to evaluate the S2m efficiency. The S2m scintillator is located behind the S0 and the gas cherenkov detectors, but in front of the lead-glass calorimeter. Therefore, for events that have a T2 trigger (S0 and gas cherenkov) and large energy deposited in the calorimeter, S2m is expected to fire as well. The procedure to calculate the S2m efficiency is as follows:

- The same tracking and PID cuts as described for the S0 efficiency are used to select a clean sample of electrons.
- Only events where the track projects inside the S2m detector are used for the efficiency calculation, as shown in figure 7. For GMp produc-

[1]It should be mentioned for completeness that on the RHRS during the GMp run, a slight X-dependence to the efficiency was found. This was due to one PMT's high voltage being set too low. However, this did not affect the elastic production data, in which the events are concentrated near the middle of the focal plane. See Appendix B for more details.

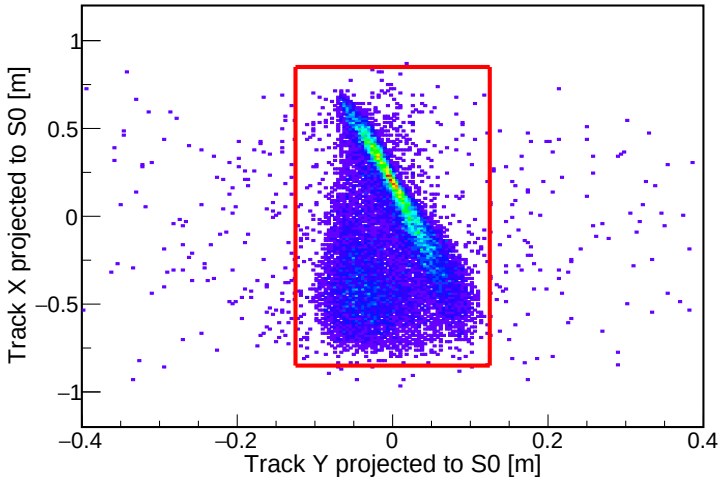

Figure 3: Good electron projection to S0 scintillator for k3-9. The red lines indicate the S0 detector edges.

tion data, an additional cut is used to select a clean sample of elastic electrons by a cut on the invariant mass as shown in figure 8.

The S2m efficiency was calculated for every production run. The efficiency was found to be stable within every individual kinematic. In addition, an inelastic run which gave reasonably uniform illumination across the focal plane was used to test the efficiency for every S2m paddle. Since the location of the S2m detector is well known, the paddle that should fire for a given event is also known (based on the track projection). Therefore the efficiency of every individual paddle can be calculated. The efficiency as a function of paddle number is shown in figure 9, after removing events with large multiple scattering between the VDC detector and S2m detector. Since the calculated efficiency is stable for all the paddles (except at the edge of the acceptance), a single efficiency was extracted for each kinematic. These efficiencies are shown in table 1.

2.3 Trigger Efficiency

The main trigger for the GMp experiment, T1, consists of a coincidence between the two scintillator detectors (S0 and S2m). There are two procedures

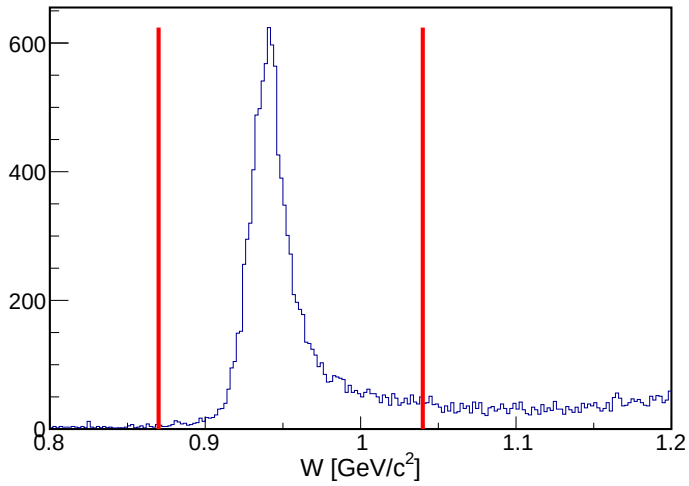

Figure 4: Additional cut used to select a clean electron sample of interest in the elastic peak ($0.87\frac{GeV}{c^2} < W < 1.04\frac{GeV}{c^2}$ for k3-9).

that can be used to calculate the trigger efficiency. In the first procedure, we can use a sample of electron events that fired either trigger T2 or T3 or both (call this sample N_T). Then, for this event sample, we can determine the number of events where trigger T1 is present (N_{T1}). If all pre-scale factors are set equal to one (as they were for GMp production data), the trigger efficiency is equal to $\frac{N_{T1}}{N_T}$. In the second procedure, one can calculate the trigger efficiency from the individual scintillator efficiencies as the product of the S0 efficiency and S2m efficiency. The trigger efficiency determined from both methods was found to be consistent. In table 2, the trigger efficiency for all kinematics is shown using the second method.

2.4 Uncertainties and Cross-Talk Check

In addition to the standard binomial uncertainty, several other factors affect the determination of the efficiency. For the individual scintillator efficiencies, the timing windows used and the knowledge of the exact positions of the scintillators relative to the VDC can have an effect. The effect on the efficiencies of changing the timing window around the main TDC peak from a very wide cut to a cut with a full-width of 200 ns is at most 5×10^{-4}. The effect on the efficiencies of changing the assumed distance of the scintillators

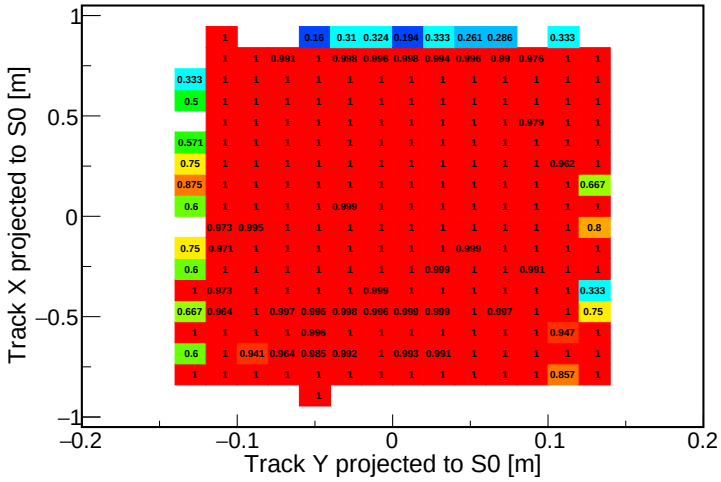

Figure 5: Two-Dimensional S0 Efficiency in bins of track projection. A LHRS inelastic run is used here.

from the VDC by 0.5 cm is about 1×10^{-3} for S0 and 5×10^{-4} for S2m. The individual scintillator efficiencies, along with the accompanying uncertainties, are shown in table 1. For the trigger T1 efficiency, in addition to the propagation of the individual scintillator uncertainties, we looked at the difference between extracting the efficiency using the two methods mentioned above. We place an uncertainty on the T1 efficiency of 1×10^{-4} on this. The trigger 1 efficiencies, along with the accompanying uncertainties, are shown in table 2.

Lastly, we looked into the question of cross-talk artificially enhancing the trigger T1 efficiency. Since all the triggers are formed by coincidences in a Majority Logic Unit (MLU), an independent method was developed to make sure that no artificial T1 signals were generated in the MLU. For every T1 event, we determined whether both S0 and S2m had signals in the TDCs for their individual channels. For all kinematics, we found that fewer than 1 in 100,000 T1 events lacked an S0 or S2m signal. So, we conclude that there was no issue with trigger cross-talk during data taking. The fact that the trigger efficiency is the same using the two methods described above demonstrates this as well.

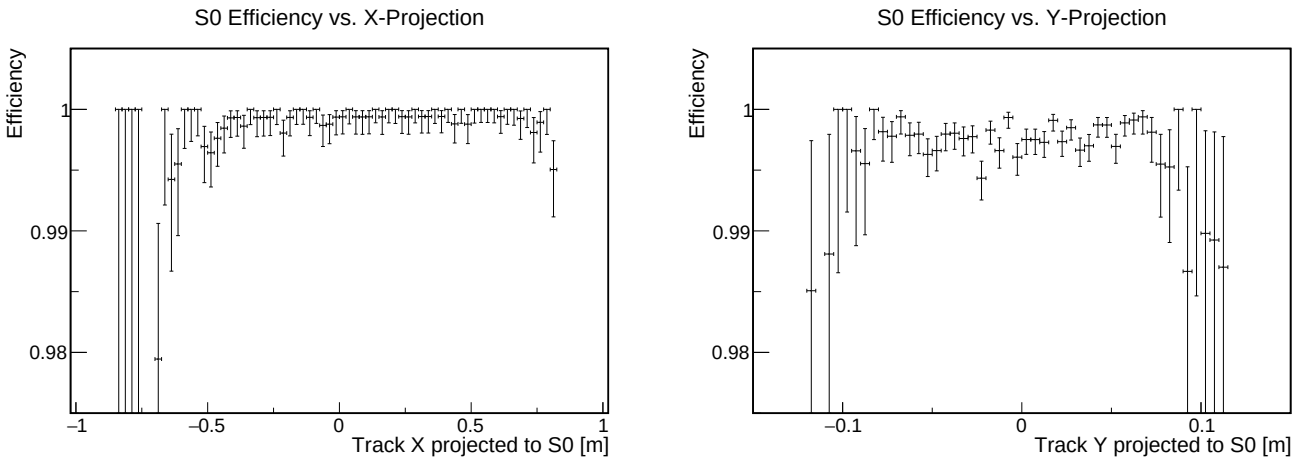

Figure 6: One-Dimensional projections of the plot in figure 5. Left: Efficiency vs. Track X Projection. Right: Efficiency vs. Track Y Projection.

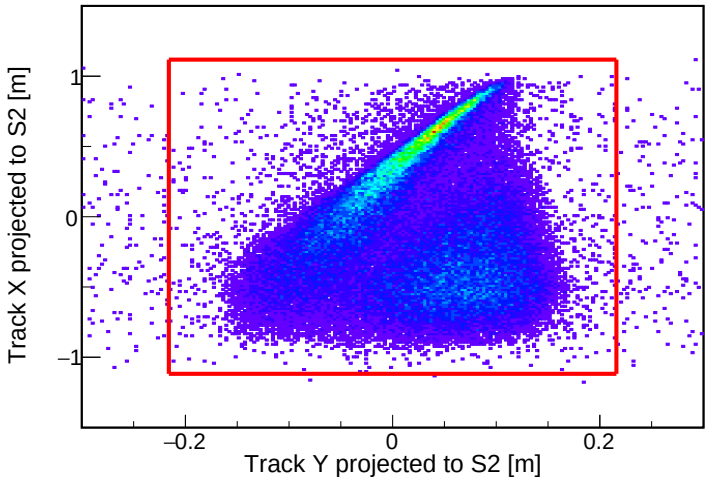

Figure 7: Good electron projection to S2m scintillator for k3-7. The red lines indicate the S2m detector edges.

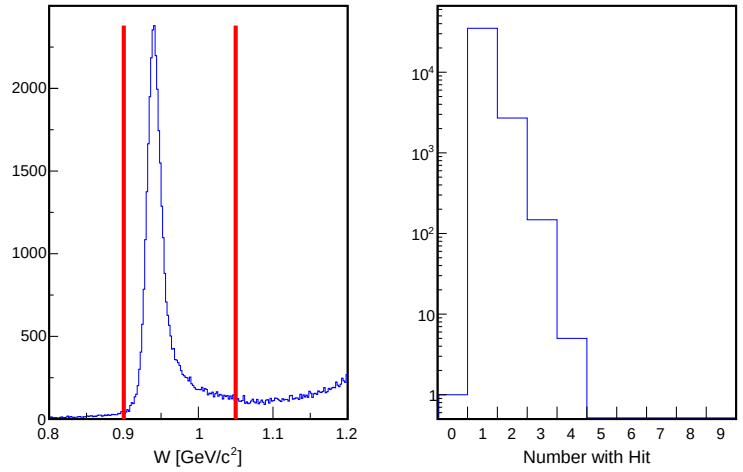

Figure 8: Left: Additional cut used to select a clean electron sample of interest in the elastic peak for k3-7. Right: Number of S2m paddles with left + right coincidence after applying all cuts. The small number of events where more than 2 paddles fire are due to the wide time window used to determine whether a PMT hit occurred.

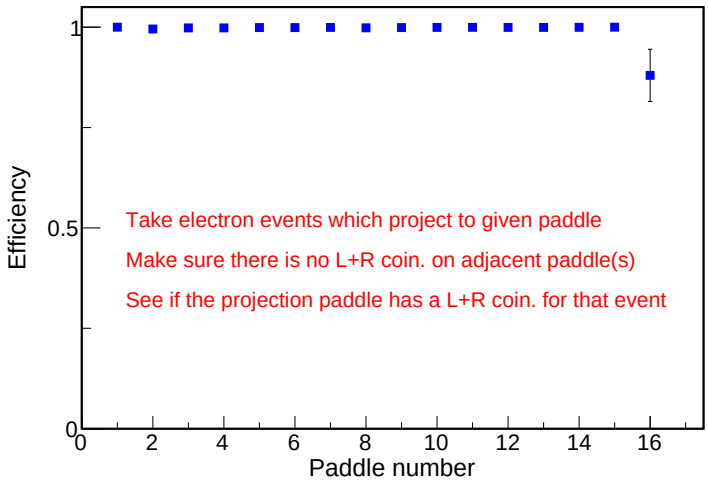

Figure 9: S2m Efficiency vs. paddle number. An inelastic run is used here. As stated on the plot, a procedure was developed to limit the effects of multiple scattering by requiring no signal on adjacent paddles.

Kinematic	Spectrometer	ϵ_{S0}	ϵ_{S2m}
k1-0.4	LHRS	0.999 (1.1×10^{-3})	0.999 (7×10^{-4})
k1-1.5	LHRS	0.999 (1.1×10^{-3})	0.999 (7×10^{-4})
k1-1.8	RHRS	0.995 (1.1×10^{-3})	0.999 (7×10^{-4})
k1-1.9	RHRS	0.998 (1.1×10^{-3})	0.999 (7×10^{-4})
k3-4	LHRS	0.998 (1.1×10^{-3})	0.999 (7×10^{-4})
k3-6	LHRS	0.999 (1.1×10^{-3})	0.999 (7×10^{-4})
k3-7	LHRS	0.999 (1.1×10^{-3})	0.999 (7×10^{-4})
k3-8	LHRS	0.999 (1.1×10^{-3})	1.000 (7×10^{-4})
k4-9	LHRS	0.998 (1.1×10^{-3})	0.999 (7×10^{-4})
k4-10	LHRS	0.998 (1.1×10^{-3})	0.999 (7×10^{-4})
k4-11	LHRS	0.999 (1.1×10^{-3})	0.999 (7×10^{-4})
k3-9	RHRS	0.996 (1.3×10^{-3})	0.999 (7×10^{-4})
k4-12	RHRS	0.995 (1.3×10^{-3})	0.999 (7×10^{-4})

Table 1: S0 and S2m efficiencies for all Fall 2016 GMp kinematics. The relative (i.e. fractional) total uncertainty for each efficiency is shown in parenthesis. The total uncertainty for each efficiency is the binomial uncertainty combined with the uncertainties discussed in the text. Each kinematic is named based on the beam energy (pass number) and the central Q^2 value.

Kinematic	Spectrometer	ϵ_{T1}
k1-0.4	LHRS	0.998 (1.3×10^{-3})
k1-1.5	LHRS	0.998 (1.3×10^{-3})
k1-1.8	RHRS	0.994 (1.3×10^{-3})
k1-1.9	RHRS	0.997 (1.3×10^{-3})
k3-4	LHRS	0.997 (1.3×10^{-3})
k3-6	LHRS	0.998 (1.3×10^{-3})
k3-7	LHRS	0.998 (1.3×10^{-3})
k3-8	LHRS	0.999 (1.3×10^{-3})
k4-9	LHRS	0.997 (1.3×10^{-3})
k4-10	LHRS	0.997 (1.3×10^{-3})
k4-11	LHRS	0.998 (1.3×10^{-3})
k3-9	RHRS	0.995 (1.5×10^{-3})
k4-12	RHRS	0.994 (1.5×10^{-3})

Table 2: Trigger 1 efficiencies calculated as the product of S0 and S2m efficiencies for all Fall 2016 GMp kinematics. The relative (i.e. fractional) total uncertainty for each efficiency is shown in parenthesis. The total uncertainty for each efficiency is the binomial uncertainty combined with the uncertainties discussed in the text. There are two methods that can be used to extract the trigger efficiency; as discussed in the text, we apply an uncertainty to account for this.

3 Particle Identification Efficiency

In many experiments, including the GMp experiment, the main trigger collects particles other than those needed for the measurement. In experiments where electrons are desired, the background particles are primarily pions and cosmic rays. To remove these background events and preserve the electrons, software cuts are applied based on the number of photoelectrons in the gas cherenkov detector and the momentum-normalized energy deposited in the calorimeter. A correction has to be made based on the number of electrons which fail the final particle identification (PID) cuts and the number of pions which pass those same cuts. (The success of all the final cuts, including tracking and timing cuts, in removing cosmic events is discussed in section 5).

The question then is what are the best quantities to extract to make this correction. We want to determine the total number of electrons, N_e^t; but what we measure before the PID cuts is $N^t = N_e^t + N_\pi^t$; after the PID cuts, we have $N^f = N_e^f + N_\pi^f$. We can determine the electron cut efficiency for the gas cherenkov (calorimeter) by selecting a sample of clean electrons in the calorimeter (gas cherenkov), and then looking at the response of the gas cherenkov (calorimeter) for that sample. We can determine the pion rejection efficiencies (i.e. the fraction that fail to pass all PID cuts) in a similar manner. Once we know the total electron efficiency (ϵ_e) and the total pion rejection efficiency (ϵ_π)[2], we can relate the yields before and after the PID cuts as $N_e^f = \epsilon_e \times N_e^t$ and $N_\pi^f = (1 - \epsilon_\pi) \times N_\pi^t$. Since we know $N^t, N^f, \epsilon_e \,\&\, \epsilon_\pi$, we can solve for $N_e^t, N_\pi^t, N_e^f \,\&\, N_\pi^f$.

However, if we write $N^f = N_e^f + N_\pi^f$ as

$$N^f = N_e^f \cdot (1 + \frac{N_\pi^f}{N_e^f}), \tag{1}$$

and the final pion-to-electron ratio, $\frac{N_\pi^f}{N_e^f}$, as $\left(\frac{\pi}{e}\right)_f$, we can solve for N_e^t as

$$N_e^t = \frac{N_e^f}{\epsilon_e \cdot (1 + \left(\frac{\pi}{e}\right)_f)}. \tag{2}$$

So, for each run we need to determine ϵ_e and $\left(\frac{\pi}{e}\right)_f$ in order to correct for

[2]Some prefer to define a pion suppression faction instead of a pion rejection efficiency; both quantities contain the same information. *De gustibus non est disputandum.*

the PID cut efficiency.

3.1 Event Categorization

In addition to the background cosmic and pion events, we found a set of events which gave a large signal in the gas cherenkov detector and no signal in the calorimeter. These events were rare compared to good events during runs with high rates, but became quite prominent at high-pass GMp production settings. The events are easily removed with a standard calorimeter cut; but since they have a large signal in the gas cherenkov, these events will artificially reduce the calorimeter efficiency that we extract using the standard method. So, prior to performing PID cut efficiency studies, we tried to better understand these events and suppress them without using the PID detectors.

In figure 10, we plot the number of photoelectrons in the gas cherenkov detector vs. the momentum-normalized total energy deposited in the calorimeter for GMp kinematic k3-7 on the LHRS. The plot is for all events with the standard trigger and a single cluster present in all 4 VDC planes. As shown on the plot, we divide the events into four categories: events with a large response in both detectors (red box), events with a large response in the cherenkov but no response in the calorimeter (green box), events with no response in the either detector (black box), and events with no response in the cherenkov but a small response in the calorimeter (blue box).

For these four categories of events, we then show in figure 11 the beta spectrum as determined from the track and scintillator timing information. As can be seen in the plot, the red and green events have similar spectra with the events peaked at beta equal to one. This, combined with the large cherenkov response, seems to indicate that the green events are actually electrons; the question is whether they are missing the calorimeter or are low-energy events produced somewhere upstream of the VDC. In the same plot, we see that the black and blue events have peaks at both positive and negative beta. The events at negative beta are cosmic events, and we cut them out by requiring $\beta > 0.2$. The remaining blue events are most likely negative pions originating from the target, while it is unclear what constitutes the black events.

To test some of the conjectures in the above paragraph, we consider several additional spectra. First, in figure 12 we plot the reconstructed target quantities for the four types of events. As can be seen, the red events fall

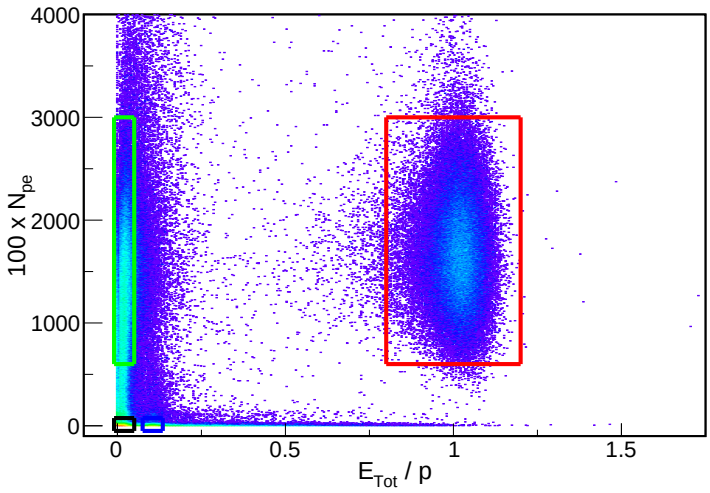

Figure 10: Gas Cherenkov vs. Calorimeter response for GMp kinematic k3-7. The meaning of the various rectangles are discussed in the text.

within the spectrometer acceptance, as expected for good electrons. A large fraction of the blue events originate from the aluminium windows of the 15 cm long hydrogen target, suggesting that these events are indeed pions. The green and the black events do not seem to track back solely to the target, which may indicate that these events do not pass through the entire spectrometer and thus are not being correctly reconstructed. These events could conceivably originate from the beam line and in-scatter into the spectrometer detector hut. However, from beam halo studies, we know that the beam is not scrapping the beam line; so the events more likely either originate from some aperture inside the spectrometer upstream of the detector hut (or, as mentioned above, are missing the calorimeter).

We can check if those events with high cherenkov response and no signal in the calorimeter are simply missing the detector. We do this by projecting the VDC track to the known position of the calorimeter. In figure 13, we show the events projected to the first layer of the calorimeter. The physical size of the calorimeter is shown by the purple box. As can be seen, the bulk of the green events fall within the calorimeter detector. So, in addition to the strange target reconstruction, there is no reason to think the green events are actually good electrons that track outside the calorimeter.

Next, we attempted to determine the origin of these background events.

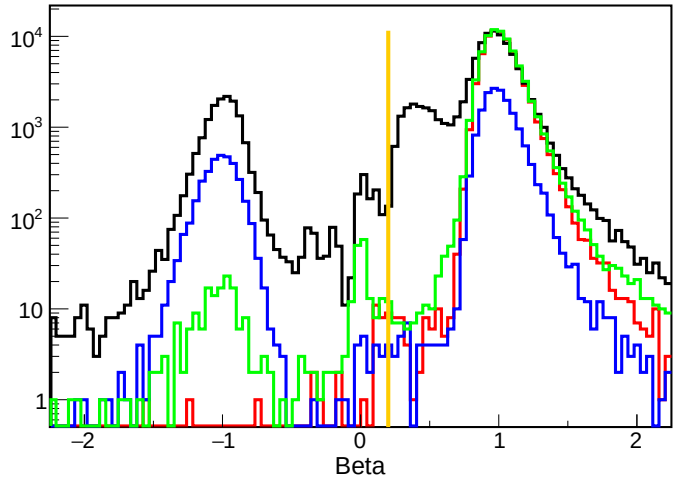

Figure 11: Beta spectra for the four types of events shown in figure 10. We apply a cut of $\beta > 0.2$ for all additional results shown in this subsection.

In figure 14, we plot the events at the VDC U1 plane. The green events consist of two bands close to the edge of the VDC in the non-dispersive direction. Although all the events are within the VDC active area, their proximity to the edge may indicate that these events are produced by an aperture somewhere near the VDC. We checked this by projecting the events forward to the second VDC plane, as well as backwards to the vacuum exit window, the end-of-bellows aperture, and the Q3 exit. Although for many of these projections some of the green events were outside the aperture, many events were situated inside the aperture. So while it was not entirely clear from where the green events originate, it is possible that the events are low-energy electrons that are produced when a high-energy particle hits an aperture near the VDC.

While it seems that no cut besides the calorimeter energy deposition can cleanly remove the background events, we can apply several cuts to significantly reduce their presence. In figure 15, we show the deviation of track projection from the center of the struck S2m paddle; requiring this deviation to be small will reduce the background events relative to the electron and pion events under study. Likewise, in figure 16, we show the deviation of the track projection from the energy-weighted hit position in the calorimeter. In figure 17, we show the reconstructed invariant mass. As can be seen, only

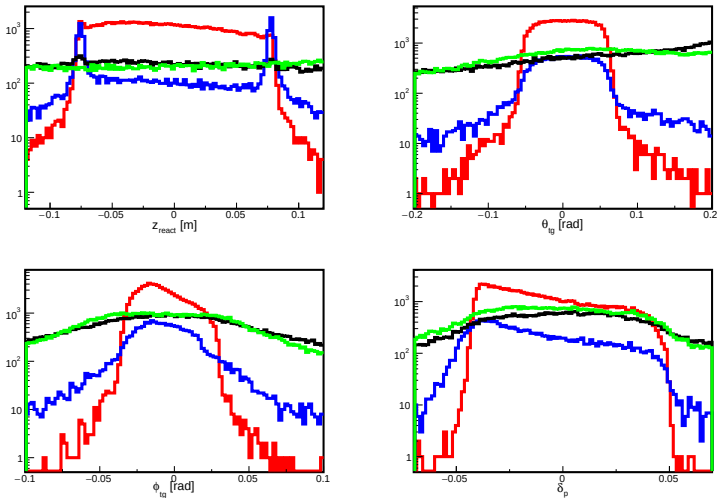

Figure 12: Reconstructed quantities for the four types of events shown in figure 10. (Clockwise from the top left: reconstructed vertex, reconstructed out-of-plane angle, reconstructed fraction momentum deviation, and reconstructed in-plane angle.)

the good electron sample shows an elastic peak. Since the GMp experiment is interested in elastic scattering, it is appropriate to apply a cut around the elastic peak when studying the PID efficiency.

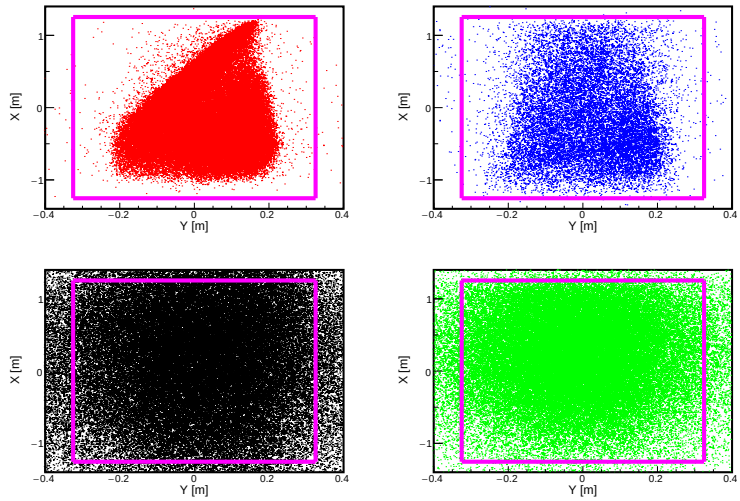

Figure 13: Track from VDC projected to calorimeter layer 1 for the four types of events shown in figure 10. The physical size of the calorimeter is shown by the purple box.

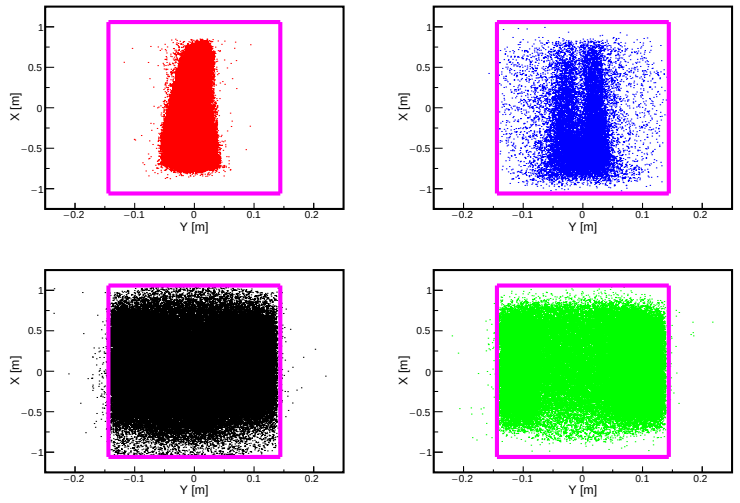

Figure 14: Track at VDC U1 plane for the four types of events shown in figure 10. The physical size of the VDC is shown by the purple box.

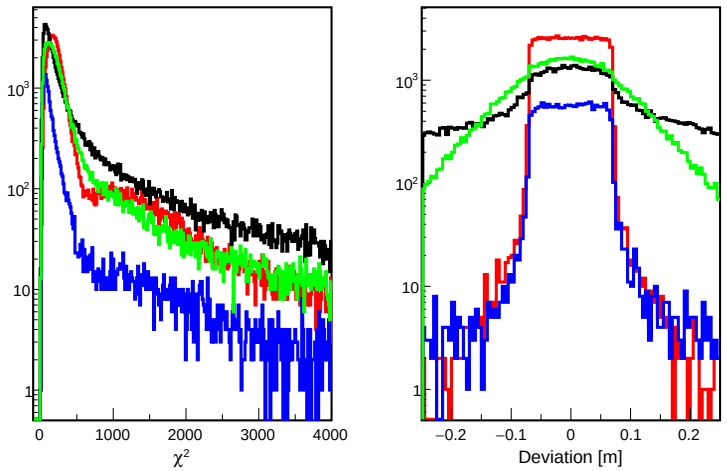

Figure 15: Right: VDC track projection deviation (in the dispersive plane) from hit S2m paddle center for the four types of events shown in figure 10. The individual S2m paddles have a full-width of 14 cm. The 'good' electron sample (red) distribution is flat from -0.7 cm to +0.7 cm, and then falls sharply. The pion distribution (blue) is also flat from -0.7 cm to +0.7 cm, but it has a larger fraction of events in the tails. The green events, however, show much less structure, which means that they experience a large amount of multiple scattering between the VDC and S2m. The is additional evidence that these events are low-energy particles. Left: VDC track quality. We don't apply any cuts on this variable for the PID efficiency study.

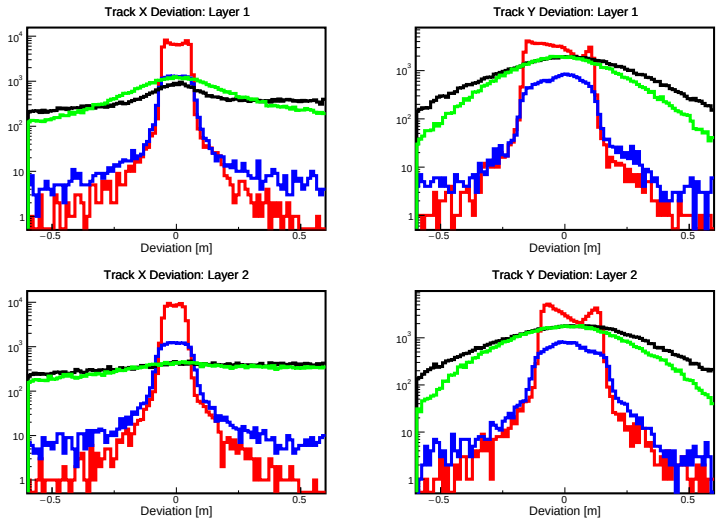

Figure 16: The VDC track projection deviation from the energy-weighted hit position in the calorimeter for both calorimeter layers and directions. The distributions are shown for the four types of events in figure 10. Since the green and black events have essentially no response in the calorimeter, the energy-weighted position for these events is just pedestal noise.

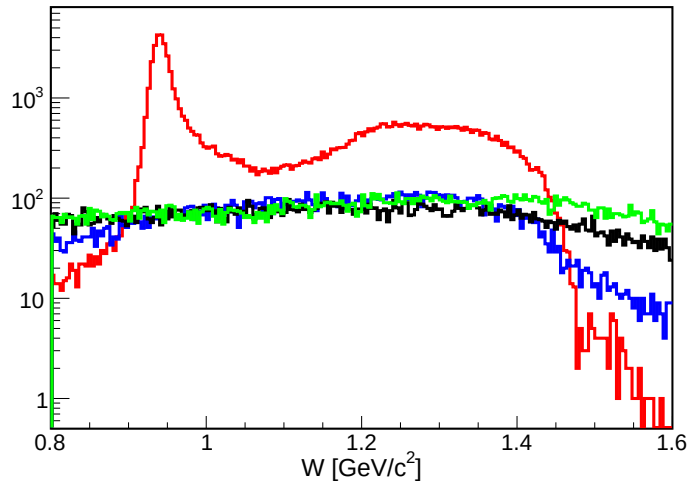

Figure 17: Reconstructed invariant mass (i.e. (e,e') missing mass) for the four types of events shown in figure 10. Only the 'good' electron (red) events display the elastic peak, as expected.

3.2 Extraction of ϵ_e and $\left(\frac{\pi}{e}\right)_f$

For the calculation of the electron efficiency and pion rejection efficiency, we begin by applying the following cuts:

1. Trigger 1 is present for the event.
2. Only 1 cluster is present in all 4 VDC planes.
3. The track beta is between 0.3 and 2.0. See figure 11.
4. The following 'sanity' cuts are applied on the acceptance (figure 12):
   - The reconstructed out-of-plane angle is between -100 mrad and +100 mrad.
   - The reconstructed in-plane angle is between -50 mrad and +50 mrad.
   - The reconstructed momentum deviation is between -5.5% and +5.5%.
   - The reconstructed reaction vertex is between -10 cm and +10 cm (-6.5 cm and +6.5 cm when calculating the electron efficiency). The hydrogen cryo-target is 15 cm long, and while many of the pion events originate from the cell windows, very few of the electrons do. So when calculating the electron efficiency, we remove the windows with a vertex cut to obtain a cleaner electron sample.
5. The absolute value of the S2m track deviation is less than 0.09 m. See figure 15.
6. The reconstructed invariant mass is between 0.8 $\frac{GeV}{c^2}$ and 1.1 $\frac{GeV}{c^2}$. See figure 17.

We should note that some of these cuts (e.g. the S2m track deviation cut) may not necessarily be used during the final cross-section extraction. They are used here in order to select the cleanest possible sample of electrons (and pions). Since the applied cuts remove electrons and pions with different probabilities, the initial pion-to-electron ratio that we extract here depends somewhat on the cuts used. However, as we show, the final pion-to-electron ratio is very small for all kinematics; and the effect of small changes to the

initial sample on the final contamination are negligible. (In addition, since many of the pion events originate from the target windows, there is probably some vertex dependence to the pion contamination which we ignore.)

For each kinematic, we first extract the software-cut-dependent electron efficiency and pion rejection efficiency for the gas cherenkov detector. We do this by selecting a clean sample of both electrons and pions based on the response in the calorimeter. In figure 18, we show the momentum-normalized energy deposition in each calorimeter layer for GMp kinematic k3-7. The selected electrons are the events contained within the red lines, while the selected pions are those within the blue lines. In the bottom left corner of the plot, one can see a small number of events which correspond to the 'low-energy' background discussed in the previous sub-section.

For the selected electron and pion samples, we plot the number of photoelectrons detected in the gas cherenkov in figure 19. Then for each possible software cut on the number of collected photoelectrons, we calculate the electron efficiency and pion rejection efficiency (figure 20). The electron efficiency is simply the fraction of the events above a given cut; the pion rejection efficiency is the fraction of events below the cut.

We repeat the process to calculate the electron efficiency and pion rejection efficiency for the calorimeter. We select a sample of electrons and pions in the gas cherenkov (figure 21), and consider their response in the calorimeter (figure 22) for GMp kinematic k3-7. However, as can be seen, both the electron and pion samples are contaminated by the 'low-energy' background discussed in the previous sub-section. To remove this background, we first isolate these events and then study the calorimeter response. The way that we isolate the 'low-energy' background events is by requiring both a large cherenkov response and a large S2m track deviation. That is, we are essentially trying to isolate the green events in figure 15, for example. After selecting these events, we then plot the calorimeter momentum-normalized energy deposition (E/p) for GMp kinematic k3-7 in figure 23. As can be seen, nearly all the events have $E/p < 0.3$. Based on this information, as well as the electron and pion peaks at lower E/p in figure 22, we choose to use only events above a certain minimum E/p when calculating the calorimeter efficiencies. When calculating the electron efficiency, we require the electron event sample to have $E/p > 0.3$; when calculating the pion rejection efficiency, we require the pion event sample to have $E/p > 0.05$.

Since there are two layers in the calorimeter, we apply a software cut on both the total energy deposited in the calorimeter and on the energy

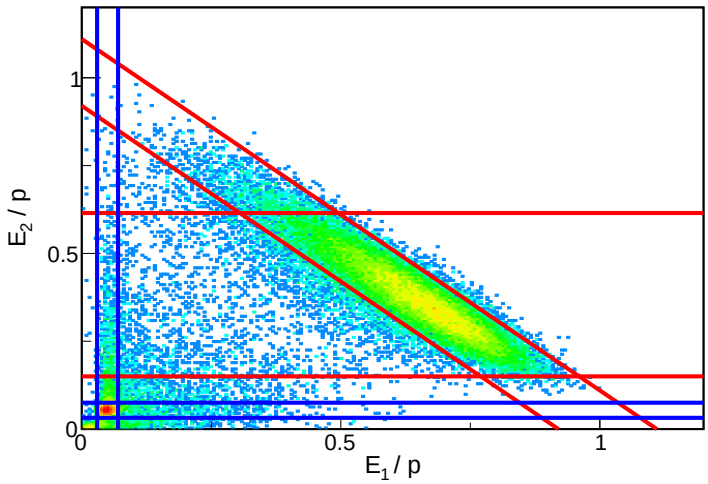

Figure 18: Electron and pion sample selection in the calorimeter for studying the gas cherenkov efficiency. The events contained within the red lines are the electrons; those contained within the blue lines are the pions. The events displayed on the plot pass the cuts listed at the beginning of this subsection. In addition, when selecting the event samples to study the gas cherenkov efficiency, we require the energy-weighted hit position in the calorimeter to be close to the track projection (see figure 16). The data shown here are for GMp kinematic k3-7.

deposited in layer 1 of the calorimeter. (The motivation for requiring a minimum energy to be deposited in layer 1 of the calorimeter comes from the vertical tail that can be seen in figure 18). In figures 24 and 25 we show grids for the calorimeter electron efficiency and pion rejection efficiency, respectively.

Similarly to what was done for the S0 and S2m scintillators, we checked for any dependence to the extracted efficiencies across the gas cherenkov and calorimeter detector planes. We did this by projecting the track to the given detector under study and looking for any dependence to the efficiency. For both the gas cherenkov and the calorimeter, the electron detection efficiency and pion rejection efficiency showed no position dependence.

The total electron efficiency is calculated from the individual cherenkov and calorimeter electron efficiencies as $\epsilon_e = \epsilon_{cer,e} \times \epsilon_{cal,e}$. The total pion rejection efficiency is calculated from the individual cherenkov and calorimeter

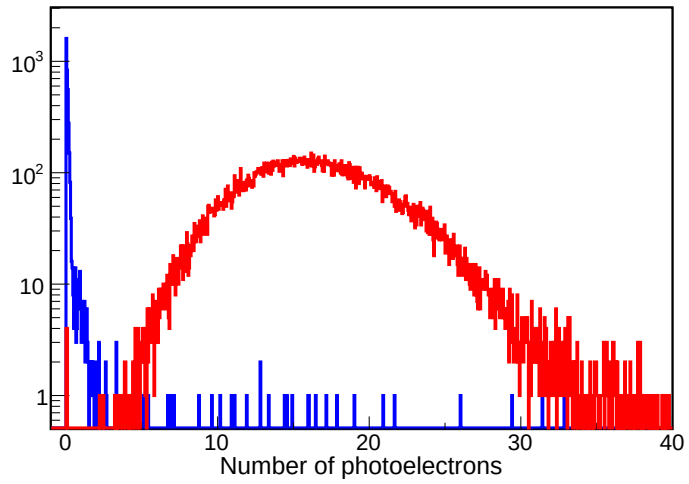

Figure 19: Number of photoelectrons collected in the gas cherenkov detector for the electron (red) and pion (blue) samples selected in figure 18.

pion rejection efficiencies as $\epsilon_\pi = 1 - (1 - \epsilon_{cer,\pi}) \times (1 - \epsilon_{cal,\pi})$. In table 3, we show the final total electron detection efficiencies, the total pion rejection efficiencies, the initial pion-to-electron ratios, and the final pion-to-electron ratios for the following set of PID cuts:

$$N_{pe} > 4,\ \left(\frac{E}{P}\right)_{Total} > 0.7,\ \left(\frac{E}{P}\right)_{Layer1} > 0.08\,.$$

We calculate a standard binomial statistical uncertainty for each measured efficiency. In addition, we consider two additional potential sources of error. First, when selecting samples of either electrons or pions in a given detector, we assume that those samples are completely 'clean' (i.e. that they only contain the particle under study). This is of course not necessarily true, and we can study the effect of contamination in the samples by varying the sample-selection cuts. Second, we make the (quite justified) assumption that all the good electron events have E/p $>$ 0.3, while all the 'low-energy' background events have E/p $<$ 0.3. We study the effect of changing this E/p threshold by a reasonable amount on the calorimeter efficiencies, and apply an uncertainty on this. The relative total uncertainties on the electron efficiencies and pion rejection efficiencies are shown in table 4.

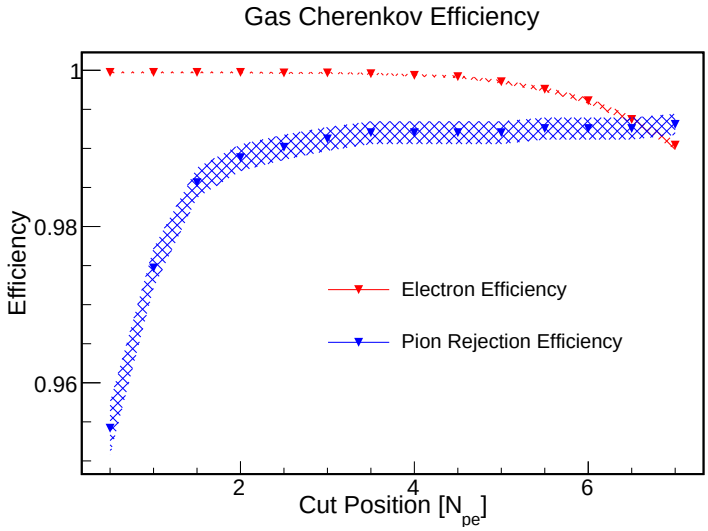

Figure 20: Electron and pion gas cherenkov cut efficiencies for the samples selected in figure 18. The error bands shown are calculated assuming standard binomial uncertainties.

As can be seen in table 3, the final pion-to-electron ratios are very small. These ratios are determined by the cut efficiencies and by the initial pion-to-electron ratio. The relative uncertainty on the final pion-to-electron ratio is also shown in table 4 for each kinematic.

Finally, we consider an alternative method for determining the PID cut efficiencies and rates of pion contamination. If one could determine functional forms for the electron, pion, and 'low-energy' background distributions in the gas cherenkov and calorimeter, all the efficiencies and pion-to-electron ratios can be easily extracted. The way to determine these spectra for a given detector would be to once again select a sample of the particle under study in the other detector. Then the resulting spectrum can be fit with an appropriate functional form. For example, one would fit the electron and pion spectra in figure 19 and then extract the efficiency for any cut. To determine the pion-to-electron ratios, one would simply scale the amplitude of the each spectrum to match the true distribution.

We attempted this fitting method, but we ran into several difficulties. We were able to fit the cherenkov spectra quite well, and the uncertainties on the extracted parameters gave uncertainties comparable to what we achieved with our cut method. For the calorimeter, however, we had to fit the good

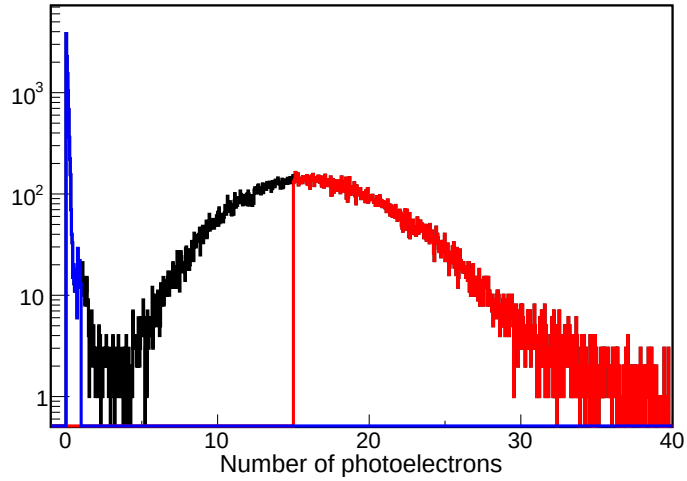

Figure 21: Electron and pion sample selection in the gas cherenkov for studying the calorimeter efficiency. Events with greater than 15 photoelectrons constitute the electron sample; those with less than 1 photoelectron constitute the pion sample. The events displayed on the plot pass the cuts listed at the beginning of this subsection. The data shown here are for GMp kinematic k3-7.

electron events and the 'low-energy' background simultaneously (see figure 22). This led to a dependence of the extracted electron efficiency on the functional form that we chose for both the electrons and the background. So we decided that the preferable method is the one discussed in detail in this section.

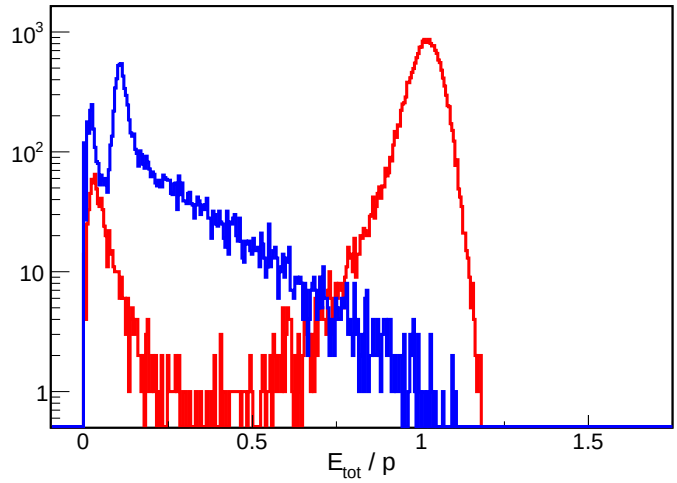

Figure 22: Total momentum-normalized energy deposited in the calorimeter for the electron (red) and pion (blue) samples selected in figure 21. As can be seen, there are clearly some events in both samples that correspond to the 'low-energy' background discussed in the last subsection. Since these events should not be included when calculating the calorimeter efficiencies, we only consider events above a certain threshold. More details are given in the text.

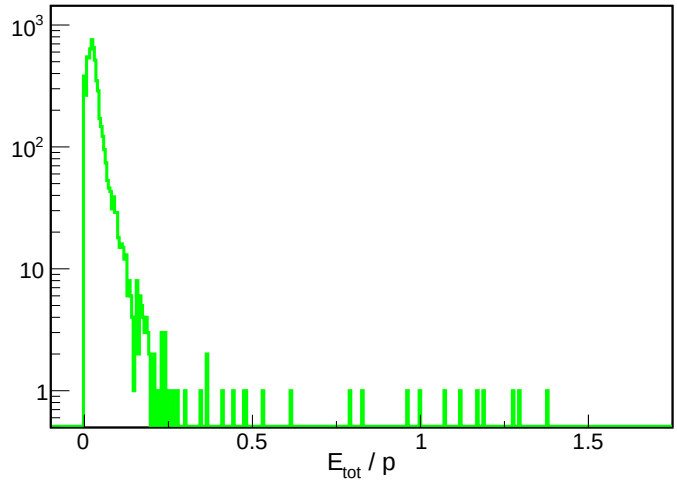

Figure 23: Total momentum-normalized energy deposited in the calorimeter for 'low-energy' background events selected by requiring a large cherenkov response and a significant amount of multiple scattering between the VDC and S2m. This plot shows us that very few of the 'low-energy' events have E/p greater than 0.3. As can be seen if figure 22, good electron events have E/p peaked at 1 with a small tail going to lower E/p. This means that we can remove the 'low-energy' contamination by requiring E/p >0.3.

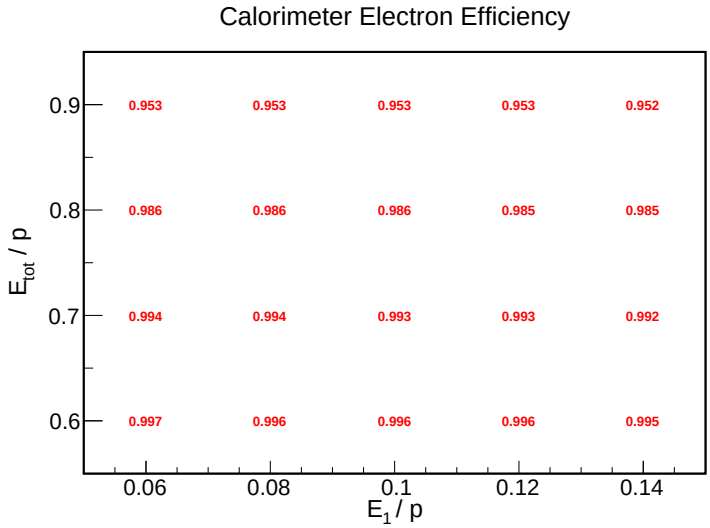

Figure 24: Grid showing calorimeter electron detection efficiencies for various cuts on the total energy deposited in the calorimeter and the energy deposited in layer 1. The results are shown for GMp kinematic k3-7.

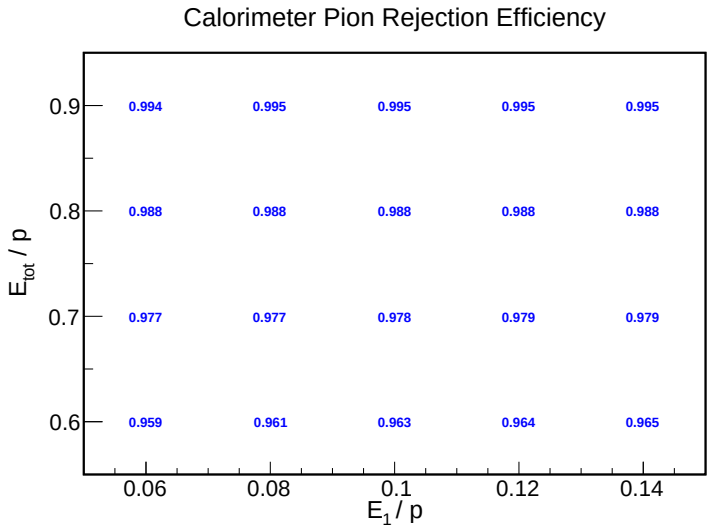

Figure 25: Grid showing calorimeter pion rejection efficiencies for various cuts on the total energy deposited in the calorimeter and the energy deposited in layer 1. The results are shown for GMp kinematic k3-7.

Kinematic	Spectrometer	ϵ_e	ϵ_π	$\left(\frac{\pi}{e}\right)_i$	$\left(\frac{\pi}{e}\right)_f$
k1-0.4	LHRS	0.995	0.977	7.4×10^{-4}	1.7×10^{-5}
k1-1.5	LHRS	0.995	0.999	9.3×10^{-4}	5.7×10^{-6}
k1-1.8	RHRS	0.992	0.999	0.025	2.9×10^{-6}
k1-1.9	RHRS	0.991	0.999	0.020	2.8×10^{-6}
k3-4	LHRS	0.992	0.999	8.7×10^{-3}	2.8×10^{-6}
k3-6	LHRS	0.993	0.999	0.057	2.3×10^{-5}
k3-7	LHRS	0.993	0.999	0.25	4.0×10^{-5}
k3-8	LHRS	0.994	0.999	1.07	1.8×10^{-4}
k4-9	LHRS	0.991	0.999	0.20	7.6×10^{-5}
k4-10	LHRS	0.992	0.999	0.55	2.3×10^{-4}
k4-11	LHRS	0.992	0.999	2.91	6.6×10^{-4}
k3-9	RHRS	0.984	0.999	7.28	4.2×10^{-4}
k4-12	RHRS	0.984	0.999	10.42	8.4×10^{-4}

Table 3: Particle identification (PID) cut efficiencies and initial and final pion contamination for all Fall 2016 GMp kinematics. The applied PID cut is discussed in the text. The initial (final) pion-to-electron ratio is defined as the ratio before (after) applying the PID cuts.

Kinematic	Spectrometer	$d\epsilon_e/\epsilon_e$	$d\epsilon_\pi/\epsilon_\pi$	$d\left(\frac{\pi}{e}\right)_f / \left(\frac{\pi}{e}\right)_f$
k1-0.4	LHRS	5.2×10^{-4}	4.5×10^{-2}	3.6×10^{-2}
k1-1.5	LHRS	5.2×10^{-4}	3.2×10^{-3}	1.1×10^{-2}
k1-1.8	RHRS	5.3×10^{-4}	1.7×10^{-3}	8.2×10^{-3}
k1-1.9	RHRS	5.4×10^{-4}	1.2×10^{-3}	1.2×10^{-2}
k3-4	LHRS	9.3×10^{-4}	1.3×10^{-2}	6.3×10^{-2}
k3-6	LHRS	7.4×10^{-4}	5.2×10^{-3}	2.1×10^{-2}
k3-7	LHRS	7.6×10^{-4}	2.1×10^{-3}	1.1×10^{-2}
k3-8	LHRS	8.4×10^{-4}	1.2×10^{-3}	8.7×10^{-3}
k4-9	LHRS	8.8×10^{-4}	3.3×10^{-3}	1.3×10^{-2}
k4-10	LHRS	8.1×10^{-4}	2.2×10^{-3}	8.4×10^{-3}
k4-11	LHRS	1.1×10^{-3}	1.4×10^{-3}	8.8×10^{-3}
k3-9	RHRS	2.0×10^{-3}	7.8×10^{-4}	1.4×10^{-2}
k4-12	RHRS	1.5×10^{-3}	5.3×10^{-4}	9.9×10^{-3}

Table 4: Relative total uncertainties on extracted electron efficiency, pion rejection efficiency, and final pion-to-electron ratio for all Fall 2016 GMp kinematics. As mentioned in the text, uncertainties are applied on the extracted electron and pion efficiencies due to the purity of the sample selection and the E/p threshold used to separate the good events from the 'low-energy' background. We apply an uncertainty of 5×10^{-4} (1×10^{-4}) on the electron (pion) efficiency due to the sample selection. We apply an uncertainty of 1×10^{-4} on both the electron and pion efficiency due to the E/p threshold.

3.3 Other Cut Efficiencies

Besides the standard PID cuts discussed in the previous subsection, an analysis may choose to apply other software cuts which require an efficiency correction. (Of course, not all software cuts require an efficiency correction. An applied cut on the reconstructed in-plane and out-of-plane angles at the target, for example, simply defines the solid angle.) For example, in the GMp experiment, it is likely that the final cross-section analysis will use a cut on the time difference between the S0 and S2m scintillators (i.e. a beta cut) to remove any remaining cosmic events. To study the efficiency of any chosen cut on the track beta, we once again begin by selecting a good sample of electron events. That is, we select events with a good trigger, a good track in the VDC, and good responses in both PID detectors. The track beta for events passing this sample-selection cut for GMp kinematic k3-7 is shown in figure 26. For a selected software cut on the track beta of greater than 0.2, we show the efficiencies for all Fall 2016 GMp kinematics in table 5.

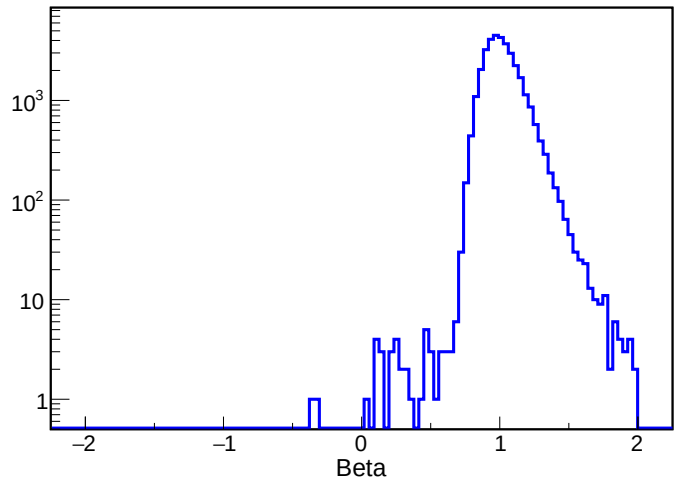

Figure 26: Track beta for a sample of good electrons selected as discussed in the text. The results are shown for GMp kinematic k3-7.

Kinematic	Spectrometer	ϵ_β
k1-0.4	LHRS	0.9999 (8×10^{-6})
k1-1.5	LHRS	0.9997 (2×10^{-5})
k1-1.8	RHRS	0.9999 (1×10^{-5})
k1-1.9	RHRS	0.9999 (2×10^{-5})
k3-4	LHRS	0.9995 (1×10^{-4})
k3-6	LHRS	0.9995 (1×10^{-4})
k3-7	LHRS	0.9997 (9×10^{-5})
k3-8	LHRS	0.9998 (9×10^{-5})
k4-9	LHRS	0.9997 (1×10^{-4})
k4-10	LHRS	0.9996 (1×10^{-4})
k4-11	LHRS	0.9998 (1×10^{-4})
k3-9	RHRS	0.9998 (2×10^{-4})
k4-12	RHRS	0.9999 (1×10^{-4})

Table 5: Track beta cut efficiency for a selected cut of beta greater than 0.2 for all GMp Fall 2016 kinematics. The relative uncertainty shown in parenthesis is the statistical (binomial) uncertainty.

4 Vertical Drift Chamber (VDC) Tracking Efficiency

For every event, the VDC can reconstruct zero, one, or multiple tracks. The 'standard' analysis method in Hall A consists of only analysing the events where the number of tracks is equal to one. Then a correction factor is applied to account for the zero-track and multi-track events: the fraction of events which consist of only one track is determined, and the yield is then divided by this value.

It is useful to briefly consider the merit of this 'one-track efficiency' approach. Let us assume that the VDC can reconstruct multiple tracks well and that the experiment taking data is not limited by statistics. Let us also assume that the experiment is interested in detecting electrons, as was the case for the GMp experiment. For a sample of events where there was a good trigger, good timing, and a large energy deposited in the PID detectors, we know that these events have at least one good electron present. The majority of the events in this sample will have one track in the VDC, and these events will be analysed. Some of the events will not have any track in the VDC. Since we know the event contained a good electron, the fact that there is no track in the VDC indicates that the detector was inefficient for that event. So a correction should be applied, as is done in the standard 'one-track efficiency' correction.

What about the cases where there are multiple tracks in the VDC? This may be because an event has multiple good electrons (a pile-up event). In the standard analysis method, this event will be thrown away; and then the 'one-track efficiency' correction will add back one of the lost electrons. The other lost electrons will be added back through the dead-time (electronic or computer) correction. Indeed, it would be a mistake to try to reconstruct two electrons in the same event, because the second electron is already counted in the dead-time correction. Multiple tracks in the VDC may also arise if there is one good electron and a 'junk' track. [3] The standard tracking correction will correct for the one good electron.

[3]This 'junk' track may be contained in the VDC; or it may be a delta-electron which escapes and either hits or misses the trigger detectors. Even if the 'junk' track hits the trigger detectors, however, it should come at the same time as the good electron track. So it will be within the electronic dead-time window, and it should not be counted by the scalers.

So the standard VDC 'one-track efficiency' correction seems justified. However, there is a complication. The newest version of the analysis software will only form two tracks when there are at least two clusters in all four VDC planes. There are some events where there are two clusters in one plane, but one cluster is the other three planes. In this case, the VDC software will reconstruct one track; but there is not always a robust way to determine which of the two clusters should be used. [4] So it might be better to throw away all events with multiple clusters in any of the four planes, and then calculate a 'one-cluster efficiency' correction. (In addition, when multiple clusters are present, the clusters may interfere with one another, and they may not be reconstructed well.)

In this section, we will calculate both the 'one-track efficiency' and the 'one-cluster' efficiency for the GMp Fall 2016 dataset. We will spend some time discussing placing reasonable uncertainties on the extracted efficiencies. In addition, we will describe a novel technique to extract position-dependent VDC efficiencies by forming a non-VDC 'track' using information from the other detectors.

4.1 Overall Efficiencies

To calculate the VDC efficiencies, we begin by selecting a sample of good electrons. First we require the event to have a good hit on the main trigger (trigger 1, which is a coincidence of the two scintillator planes). Then we require at least 5 photoelectrons in the gas cherenkov detector. Lastly we apply a cut on the energy deposited in the calorimeter normalized by the spectrometer central momentum. It is important to highlight the reason that we divide the energy deposited in the calorimeter by the spectrometer central momentum instead of the event momentum, as we did in previous sections. The event momentum is calculated using the central momentum and information from the reconstructed VDC track. Using VDC information when creating a sample to study the VDC efficiency would obviously bias our study. By normalizing the calorimeter energy deposition by a fixed number (the spectrometer central momentum), we avoid this particular pitfall.

Now that we have a sample of good electrons, we can calculate the fraction of these events with one track in the VDC or one cluster in all four VDC

[4] Of course, the VDC software could be changed to reconstruct two tracks here. But this is just a semantic issue, as it would change the 'one-cluster efficiency' into the 'one-track efficiency'.

planes. But we first make use of two additional pieces of information to remove any potential cosmic contamination or events which miss the VDC detector entirely: the relative time in the two scintillator planes, and the hit positions of the event in the two scintillator planes.

The S0 and S2m scintillators have been well calibrated, with regards to their relative times and their positions with respect to the VDC. For every event, we can extract the (X,Y,Z) hit positions for each scintillator. For the S2m scintillator, the Z position relative to the VDC is known; we can set the X position as the center of the S2m paddle that had a hit; and we can use the time difference between the left and right PMTs of the hit paddle to determine the Y position. For the S0 scintillator, the Z position relative to the VDC is known; we can set the Y position as the center of the S0 detector; and we can use the time difference between the top and bottom PMTs to determine the X position. Using the extracted (X,Y,Z) hit positions for the two scintillator detectors, we form a 'track' (i.e. non-VDC track).

Using the scintillator relative times and the scintillator-based track, we calculate a beta for every event (figure 27). (If multiple S2m paddles fire, we use the earliest one that was within a 50 ns time window of the S0 hit.) As can be seen in the plot, even after the PID cut, there are a few events with negative beta. We remove these events by requiring the beta to be larger than 0.4 and less than 2.0.

We can also form the standard focal plane tracking variables in the transport coordinate system using the scintillator-based track. We can then remove events from our sample which track far outside the acceptance of the VDC detector. In figure 28, we show these four quantities formed with the scintillator-based track, both for all trigger 1 events and for those events passing the above PID and beta cuts. After applying the PID and beta cuts, it is clear that very few events are left which are outside the VDC fiducial region. Nonetheless, we apply cuts to remove the small number of events which are far outside the VDC acceptance.

We use the sample of events remaining after applying the PID, beta, and scintillator-based tracking cuts to study the VDC efficiency. That is, we calculate the fraction of these events that have one-track or one-cluster present in the VDC. Figure 29 shows the number of tracks reconstructed by the VDC for the selected event sample for an inelastic run on the LHRS.

In table 6, we show the extracted VDC one-track and one-cluster efficiencies for all GMp Fall 2016 kinematics. In addition, the table shows the statistical uncertainty placed on the efficiencies assuming standard binomial

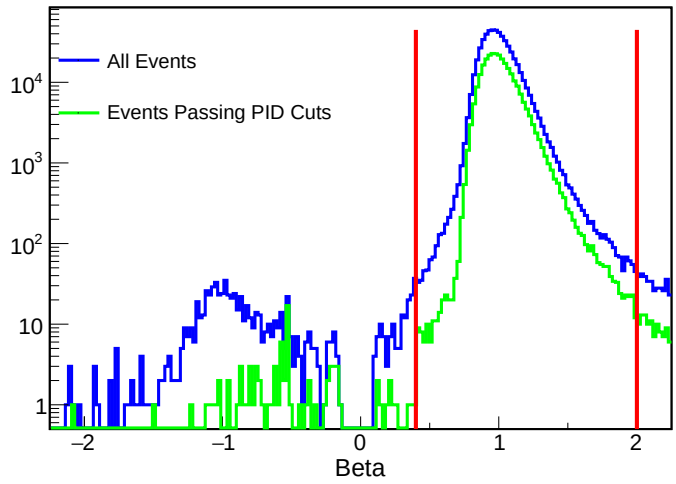

Figure 27: Beta formed from the scintillator times and path-length of the scintillator-based track. The blue curve shows all trigger 1 events. The cosmic events are the ones with negative beta. The green curve shows the distribution for the events remaining after the application of the PID cuts discussed in the text. The PID cuts remove the majority of the cosmic events. Note how there are no events with $-0.1 < \beta < 0.1$; this occurs because we require the S0 and S2m hit times to be within 50 ns of each other. The results are shown for an inelastic run on the LHRS.

uncertainties. We place an additional uncertainty of 0.2% on all extracted VDC efficiencies. This additional uncertainty is needed to take into account the fact that the fraction of one-track or one-cluster events in the physics region of interest may be different from the fraction of multi-track or multi-cluster events in that same region. See [5] for a more complete discussion.

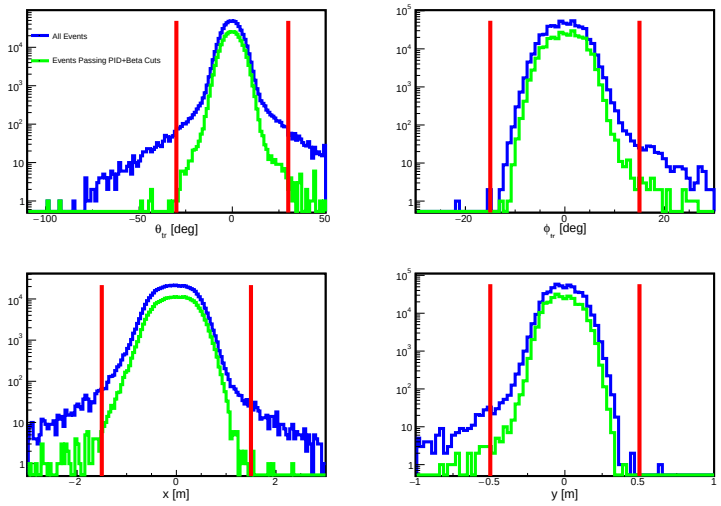

Figure 28: The standard focal plane variables in the transport coordinate system formed from the scintillator-based track. (Clockwise from the top left: angle in the dispersive direction, angle in the non-dispersive direction, position in the non-dispersive direction, position in the dispersive direction.) The blue curves show the distributions for all trigger 1 events. The green curves show the distributions after applying the PID and beta cuts discussed in the text. For the green curves, a few events reconstruct far outside the known VDC acceptance; these events are removed with the cuts shown in the figure. The results are shown for an inelastic run on the LHRS.

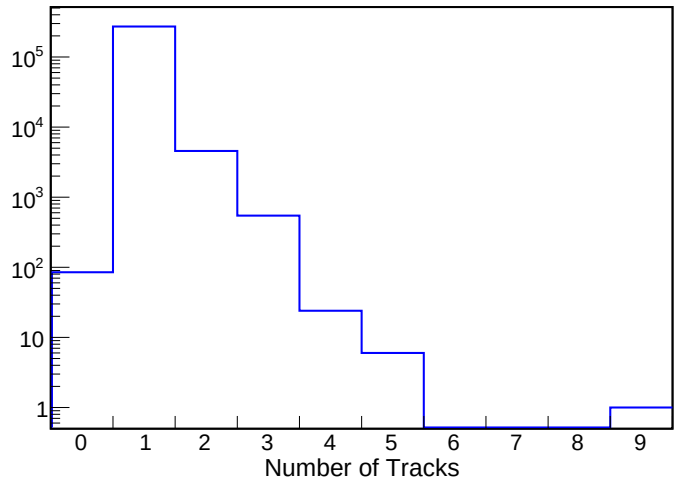

Figure 29: Number of tracks reconstructed by the VDC for a sample of good electrons. The results are shown for an inelastic run on the LHRS.

Kinematic	Spectrometer	$\epsilon_{1-track}$	$\epsilon_{1-cluster}$
k1-0.4	LHRS	0.9899 (9.6×10^{-5})	0.9282 (2.6×10^{-4})
k1-1.5	LHRS	0.9913 (9.6×10^{-5})	0.9244 (2.9×10^{-4})
k1-1.8	RHRS	0.9940 (9.7×10^{-5})	0.9242 (3.5×10^{-4})
k1-1.9	RHRS	0.9940 (1.3×10^{-4})	0.9244 (4.8×10^{-4})
k3-4	LHRS	0.9728 (6.5×10^{-4})	0.8886 (1.37×10^{-3})
k3-6	LHRS	0.9770 (4.9×10^{-4})	0.9016 (1.06×10^{-3})
k3-7	LHRS	0.9800 (5.1×10^{-4})	0.9107 (1.11×10^{-3})
k3-8	LHRS	0.9846 (5.6×10^{-4})	0.9171 (1.35×10^{-3})
k4-9	LHRS	0.9726 (4.1×10^{-4})	0.8949 (1.27×10^{-3})
k4-10	LHRS	0.9744 (4.0×10^{-4})	0.9015 (1.27×10^{-3})
k4-11	LHRS	0.9793 (6.0×10^{-4})	0.9095 (1.27×10^{-3})
k3-9	RHRS	0.9905 (7.4×10^{-4})	0.9195 (2.24×10^{-3})
k4-12	RHRS	0.9833 (7.5×10^{-4})	0.9118 (1.80×10^{-3})

Table 6: Extracted VDC one-track and one-cluster efficiencies for all GMp Fall 2016 kinematics. The relative uncertainty shown in parenthesis is the statistical (binomial) uncertainty. As discussed in the text, we suggest placing an additional uncertainty of 0.2% on these values.

4.2 Position-Dependent Efficiency

While the procedure we developed in the previous section works well for calculating the overall VDC efficiency, the scintillator-based track is not adequate for calculating efficiencies as a function of position in the VDC detector. The reason for this can be seen in figure 30. In this figure, we take events in which a good track was reconstructed in the VDC. We then project the VDC track to the S0 (S2m) detector plane, and we compare this track's X (Y) position in the S0 (S2m) plane to the X (Y) position given by the time difference of the S0 (S2m) PMTs. The X position we get by using the S0 PMT time difference can differ from the X position of the VDC track projection by up to 10 cm. For S2m, the PMT-based Y position can differ by 5 cm from that of the VDC track projection. Since the VDC tracks are reconstructed with a high accuracy, this large discrepancy is mostly due to the time resolution of the scintillators (and also perhaps to some multiple scattering between the VDCs and the scintillator detectors).

Thankfully, additional position information from other detectors can be used to form a more accurate non-VDC-based track. In the calorimeter, we have access to the energy-weighted X and Y hit positions in both layers (figure 31). In the straw chambers, we can extract X and Y positions based on which straws had signals for that event (figure 32).

So we have five potential sets of (X,Y,Z) values for each event: one from S0, one from S2m, two from the calorimeter (since there are two layers), and one from the straw chamber. Since we have already imposed the requirement that trigger 1 is present and that there is a large amount of energy deposited in the calorimeter (i.e. the PID cuts), we are guaranteed to have at least four (X,Y,Z) values for every event. (If there are multiple clusters in the calorimeter, we take the one with the largest energy deposition.) When the event has one cluster in the straw chamber, we include the (X,Y,Z) hit information from the straw chamber; if the straw chamber has zero or multiple clusters, we do no use the straw chamber information. We weight each used X and Y position based on its accuracy (as determined from figures 30 - 32), and we perform a least-squares fit to determine a track.

Figure 33 compares the non-VDC-based track to the standard VDC track for events with one cluster in all four VDC planes. The figure shows the difference between the non-VDC-based track and the standard VDC track for the four focal plane quantities in the transport coordinate system. The blue curves show the differences between the non-VDC-based track and the

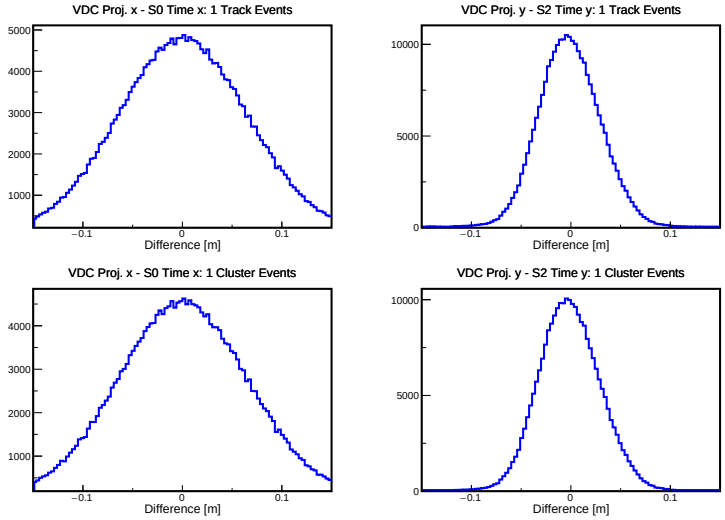

Figure 30: Top/Bottom Left: Difference between the VDC track projection to the S0 scintillator in the X direction and the position determined by the S0 PMT times. The top plot is shown for events with one track in the VDC; the bottom plot is shown for events with one cluster in all four VDC planes. Top/Bottom Right: Difference between the VDC track projection to the S2m scintillator in the Y direction and the position determined by the S2m PMT times of the struck paddle. The top plot is shown for events with one track in the VDC; the bottom plot is shown for events with one cluster in all four VDC planes.

standard VDC track when only the two scintillators are used to form the non-VDC-based track; the red curves show the differences when the two scintillators and the calorimeter are used to form the non-VDC-based track; the green curves show the differences when the non-VDC-based are formed as described in the previous paragraph. As can be seen in the figure, the resolution on the green curves is quite good. (In figure 34, we show the same differences as in figure 33 for the final non-VDC-based track, but this time as a function of position in the VDC detector.)

The upshot of all this is the following: for a sample of good electrons selected by the trigger and PID detectors, we can form a non-VDC-based track using the scintillators, the calorimeter, and (usually) the straw chamber. We can then bin that sample across the entire VDC detector and study the one-track and one-cluster efficiency of the VDC in different parts of the

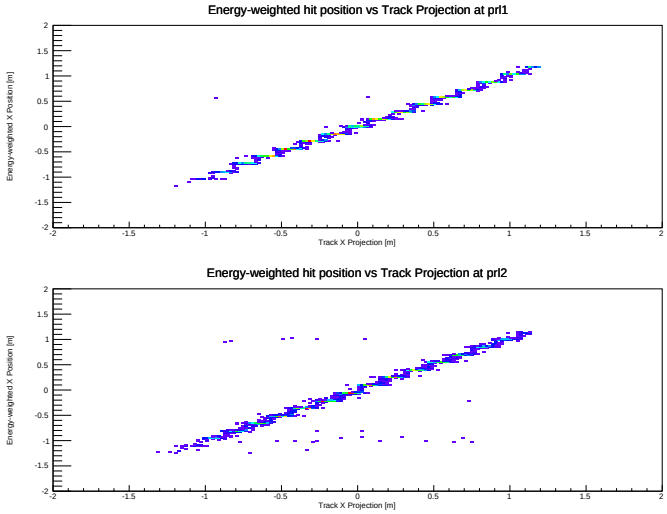

Figure 31: The energy-weighted X position of the largest-energy cluster in the calorimeter vs. the VDC track X projection to the calorimeter. Since the extracted energy-weighted position is consistent with the VDC position (within resolution), the energy-weighted position can be used when calculating the non-VDC-based track. The top plot is for calorimeter layer 1, while the bottom plot is for calorimeter layer 2. The results are shown for a LHRS inelastic run.

detector. We do this as a function of the X and Y position in the focal plane transport coordinate system in figures 35 and 36 for an inelastic run on the LHRS. As can be seen in figure 36, the one-cluster efficiency shows a minor dependence on X. (The full rotated width of the VDC in the X direction in the transport coordinate system is 156 cm.) It appears that the efficiency shows a major dependence on Y. However, while the full physical width of the VDC in the Y direction is 30 cm, the vast majority of the events fall within about 8 cm of the center of the VDC for the run studied, as can be seen in figure 34. In this narrow window, the efficiency is very stable.

The technique we described in this section can be used to extract position-dependent VDC efficiencies in many situations. However, we do not think it is correct to apply the curves in figure 36 as a general efficiency correction. The VDC one-track and one-cluster overall efficiency will change with the event rate, and the shape of the efficiency curve across the VDC may be affected by the relative event rate. For experiments, like GMp, where the

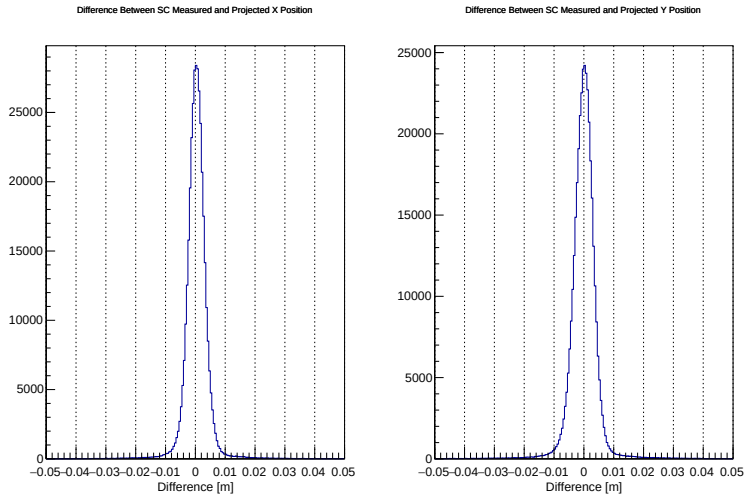

Figure 32: Left (Right): The difference between the position extracted from the straw chamber in the X (Y) direction minus the position of the VDC track projected to the straw chamber. The extracted positions are consistent to better than 1 cm. This means that the straw chamber hit information can be used when forming a non-VDC-based track. The results are shown for events with a single track in the VDC and a single cluster in the straw chamber. The straw chamber geometry consists of 3 parallel layers followed by an additional 3 layers perpendicular to these; so we assume that all straw chamber hits occur at the center of the detector in the Z direction when calculting the hit X and Y positions. The results are shown for a LHRS inelastic run.

events of interest are rather localized at the focal plane, a single number for the VDC efficiency correction is probably sufficient.

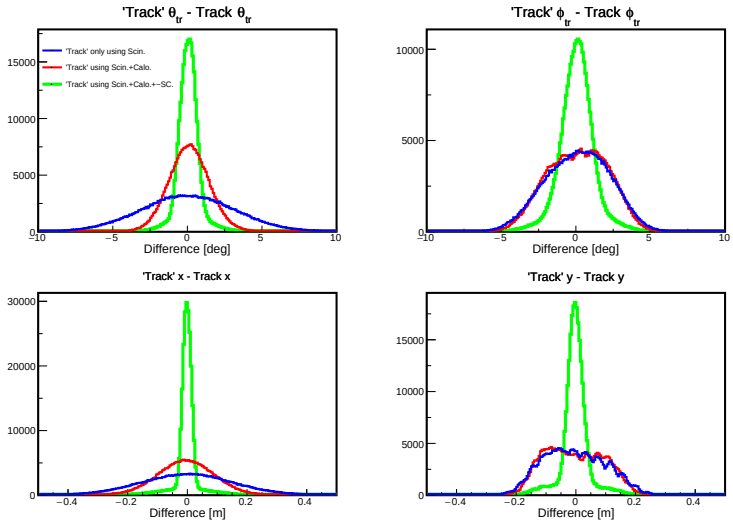

Figure 33: The difference between the standard focal plane variables in the transport coordinate system formed from the non-VDC-based track and those formed from the standard VDC track. (Clockwise from the top left: difference in the angle in the dispersive direction, difference in the angle in the non-dispersive direction, difference in the position in the non-dispersive direction, difference in the position in the dispersive direction.) As discussed in the text, the blue curve shows the difference when only the two scintillators are used to form the non-VDC-based track. The red curve shows the difference when the calorimeter information is included in addition. The green curve shows the difference when the straw chamber information is included as well, if a single cluster is present in the straw chamber. The results are shown for an inelastic run on the LHRS.

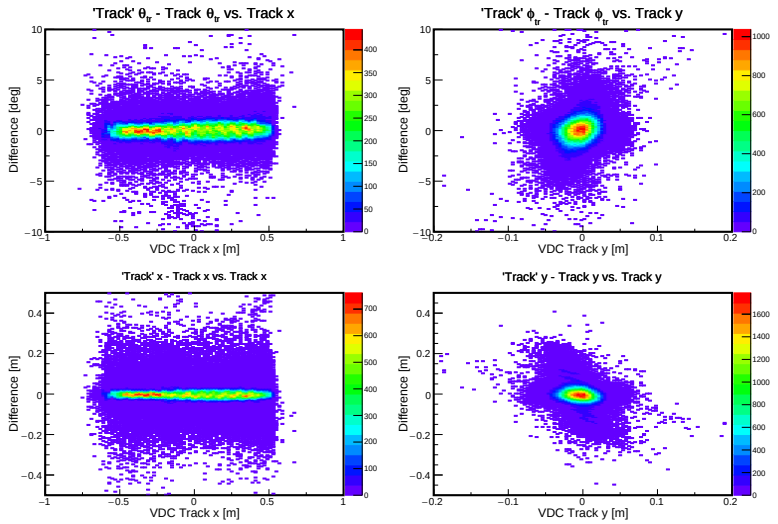

Figure 34: The difference between the standard focal plane variables in the transport coordinate system formed from the non-VDC-based track and those formed from the standard VDC track vs. the position in the VDC (as determined from the standard VDC track). (Clockwise from the top left: difference in the angle in the dispersive direction vs. the position in the dispersive direction, difference in the angle in the non-dispersive direction vs. the position in the non-dispersive direction, difference in the position in the non-dispersive direction vs. the position in the non-dispersive direction, difference in the position in the dispersive direction vs. the position in the dispersive direction.) The results show that the final non-VDC-based track is accurate across the entire VDC detector. The results are shown for an inelastic run on the LHRS.

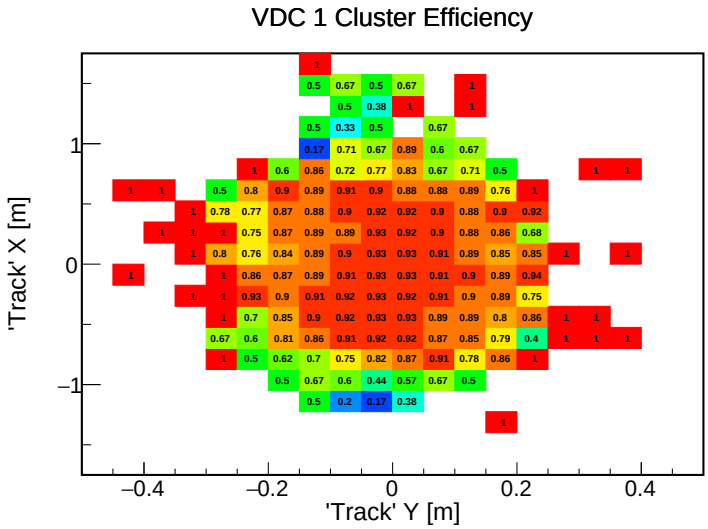

Figure 35: Fraction of the good electron events which contain one cluster in all four VDC planes as a two-dimensional function of position at the VDC. The data is binned in X vs. Y in the focal plane transport coordinate system using the non-VDC-based track, and an efficiency is calculated for each bin. The results are shown for an inelastic run on the LHRS.

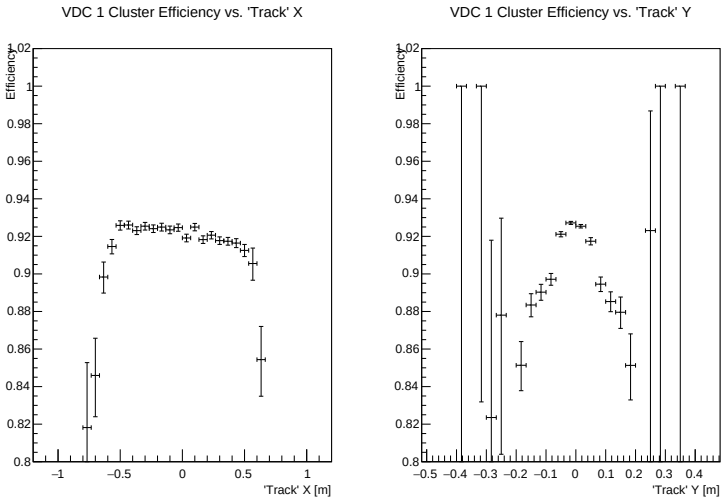

Figure 36: Left (Right): Fraction of the good electron events which contain one cluster in all four VDC planes as a function of the X (Y) position at the VDC. The data is binned in X (Y) in the focal plane transport coordinate system using the non-VDC-based track, and an efficiency is calculated for each bin. The results are shown for an inelastic run on the LHRS.

5 Cosmic Suppression

As mentioned in previous sections, the main trigger for the GMp experiment was Trigger 1 (T1), a coincidence of the two scintillator detectors (S0 and S2m). This trigger collected cosmic events at a raw rate of approximately 5 Hz. Since the GMp experiment took data for over a month, it is important to determine whether any cosmic contamination is present in the data after the application of our final software cuts. During the experiment, we were able to take a 33 hour cosmic run on the LHRS (i.e. a run where we collected data in the same way as during production running, but no beam was present in the experimental hall). We can use this run to study our success in suppressing cosmic contamination with our software cuts.

For this cosmic run, figure 37 shows the beta distribution for T1 events. The beta is calculated using the relative time between the two scintillator detectors and the scintillator-based track described in section 4. The vast majority of events have a negative beta peaked at -1, as expected (i.e. the cosmic event first hits S2m and then hits S0). However, there are a few events peaked around beta equal to +1. Since at this point we only require the two scintillator detectors to have a signal, these events may be ones that first hit the top of the S0 detector before striking the S2m detector. In figure 38, we plot the beta vs. the angle in the dispersive direction (i.e. the vertical direction) for the same events as shown in figure 37. As can be seen in figure 38, the events with negative beta have a negative angle. This is consistent with the events hitting S2m at a higher part of the detector than S0. (Remember that +X is down, and +Z points from S0 to S2m.) The events with positive beta tend to have a positive angle. This suggests that these events hit S0 higher than S2m.

In any case, the important question for us is what happens when we apply cuts on the VDC and the PID detectors. In figure 39, we plot the beta distribution for the cosmic run under study after applying cuts on the VDC and PID detectors. We require a single cluster to be present in all four VDC planes, and we require 5 photoelectrons in the gas cherenkov detector. In addition, we require the total energy deposited in the calorimeter to be greater than 510 MeV. This is equivalent to requiring a momentum-normalized energy deposition of 0.6 if the central momentum is 850 MeV/c. (For the GMp production data, the set momentum was always greater than 1 GeV/c; so what is shown here is a worst-case scenario.) As can be seen in the figure, there are still approximately 100 events remaining after the VDC and PID

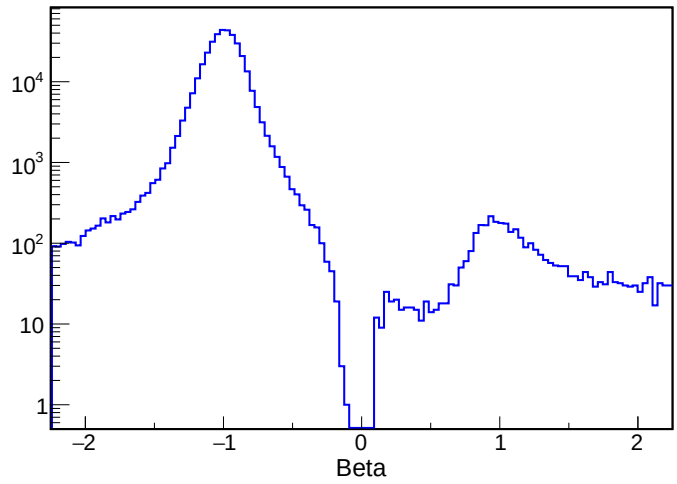

Figure 37: Beta calculated from the scintillator times and scintillator-based track for a cosmic run on the LHRS. The vast majority of events have a negative beta. A few events have positive beta; the origin of these events are discussed in the text. The two vertical red lines indicate a beta cut that is sometimes applied during the analysis of the production data.

cuts. However, they are all at negative beta.

We can conclude that the combination of trigger, VDC, PID, and beta cuts are sufficient to remove all cosmic events over a 33 hour period. The higher Q^2 GMp kinematic settings took data for approximately a week, and accumulated about 10,000 good electrons during that time. In addition to the cuts discussed here, software cuts are applied on the reconstructed target quantities and the invariant mass. These cuts would further reduce the cosmic contamination. Furthermore, these higher Q^2 kinematics had central momentum settings of around 2 GeV/c; thus the applied calorimeter energy deposition cut is higher than the one used in this study. So it is justified to claim that the final cosmic contamination is less than 5×10^{-4}.

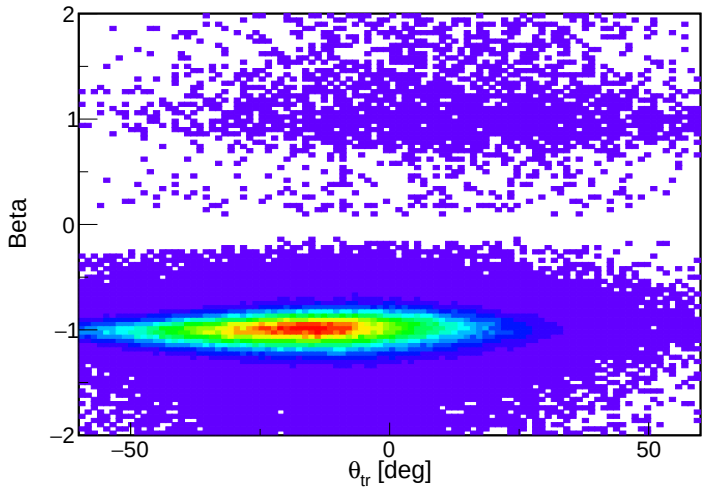

Figure 38: Beta vs. angle in the dispersive direction. The angle is calculated using the scintillator-based track. The events shown here are the same ones in figure 37. The coordinate system used to define the angle is the spectrometer transport coordinate system. So a positive angle means that the event hit the S0 detector vertically higher than the S2m detector (+X points down).

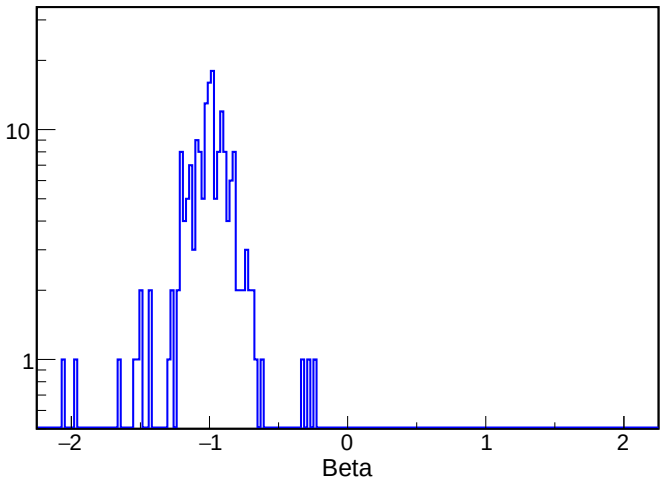

Figure 39: Beta distribution for cosmic events on the LHRS after applying the tracking and PID cuts discussed in the text. There are 100 or so events left in the plot, all at negative beta.

6 Computer and Electronic Live-Time

When an event triggers the data-acquisition system, another event can not be processed for some time. We need to correct for the number of events lost during this time period. Because the events which occur during the period when the data-acquisition is down are still recorded on the scalar counters, we define the computer live-time as the ratio of the number of events recorded for the main trigger divided by the number of counts on the main trigger scalar. The measured yield then needs to be divided by the computer live-time to correct for the lost time. (For the GMp experiment, the pre-scale factor for the main trigger was always set to one during production running. If this were not the case, we would need to take this into account in our calculation.) In table 7, we show the computer live-time for all GMp Fall 2016 kinematics, along with the accompanying relative uncertainties calculated assuming binomial errors.

Kinematic	Spectrometer	Computer Live-Time
k1-0.4	LHRS	0.6935 (5.1×10^{-4})
k1-1.5	LHRS	0.9454 (2.2×10^{-4})
k1-1.8	RHRS	0.9171 (3.3×10^{-4})
k1-1.9	RHRS	0.9207 (5.1×10^{-4})
k3-4	LHRS	0.9654 (4.2×10^{-4})
k3-6	LHRS	0.9774 (3.1×10^{-4})
k3-7	LHRS	0.9794 (1.1×10^{-4})
k3-8	LHRS	0.9843 (3.0×10^{-4})
k4-9	LHRS	0.9742 (2.5×10^{-4})
k4-10	LHRS	0.9728 (2.6×10^{-4})
k4-11	LHRS	0.9790 (3.6×10^{-4})
k3-9	RHRS	0.9684 (5.4×10^{-4})
k4-12	RHRS	0.9547 (6.5×10^{-4})

Table 7: Extracted computer live-times for all GMp Fall 2016 kinematics. The relative (i.e. fractional) uncertainty shown in parenthesis is calculated assuming binomial errors.

In addition, there is a set of events that are not recorded on the scalar counters. These lost events are due to the electronic dead-time. For every recorded event, the number of lost events is equal to $Rate \times \tau$, where $Rate$

is the raw event rate on the scalar counters and τ is the electronic dead-time. To correct for this electronic dead-time, the measured yield should be multiplied by the following factor:

$$Correction\,Factor = 1 + Rate \times \tau\,.$$

One way to estimate the correction factor is to use multiple coincidence units with different output widths [6]. In our case, we make use of the fact that we have multi-hit TDCs. Figure 40 shows the TDC time (relative to a common start) for the main trigger when two hits are present. The vertical axis is the earlier hit, and the horizontal axis is the later hit. The vertical band in the figure shows events for which earlier hit came prior to the data acquisition system being ready to accept an event. The horizontal band represents events for which the earlier hit carried the time. By examining the gap in the middle of the figure, we can conclude that the electronic dead-time (τ) is about 40 ns.

In figure 41, we plot the correction factor as a function of rate for a 40 ns electronic dead-time. For GMp Fall 2016 production running, the raw rate was always below 6 kHz (usually below 1 kHz). This means the correction due to the electronic dead-time is at most 2×10^{-4}.

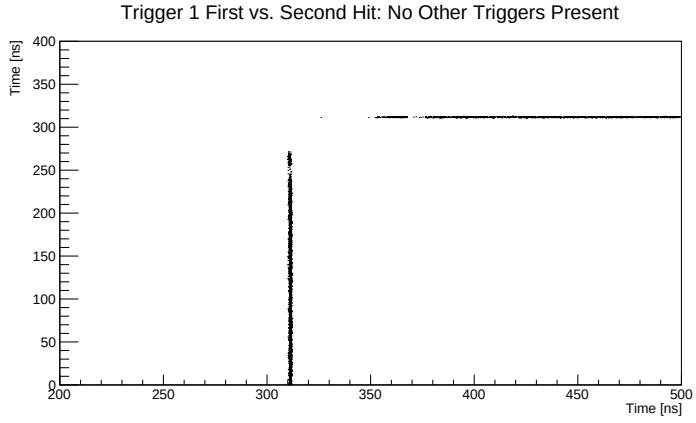

Figure 40: Main trigger TDC times for events with two hits. The interpretation of the figure is discussed in the text.

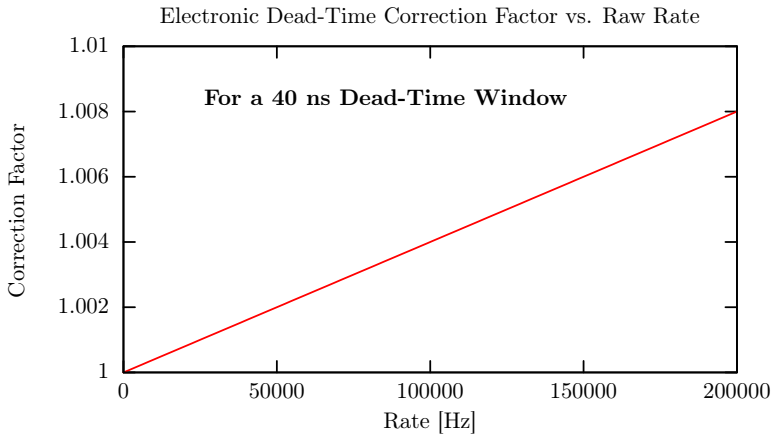

Figure 41: Electronic dead-time correction factor vs. raw rate. The plot is made assuming a 40 ns electronic dead-time. The measured yield should be multiplied by this correction factor.

Appendix

A Analysis Code

Analysis codes exist for calculating each efficiency described above. The codes can be provided at request to the authors: Barak Schmookler & Bashar Aljawrneh .

B Fall 2016 RHRS S0 Scintillator Inefficiency

As discussed in section 2, the RHRS S0 had a position-dependent inefficiency during the Fall 2016 running. This was due to one of the PMTs inadvertently having a slightly low HV applied to it. While the problem does not affect the elastic data, anyone wishing to analyse inelastic data during the Fall 2016 run period should apply a position-dependent efficiency correction for S0. For this purpose, we analysed an inelastic run on the RHRS and parametrized the efficiency using a 3^{rd} order polynomial (figure 42).

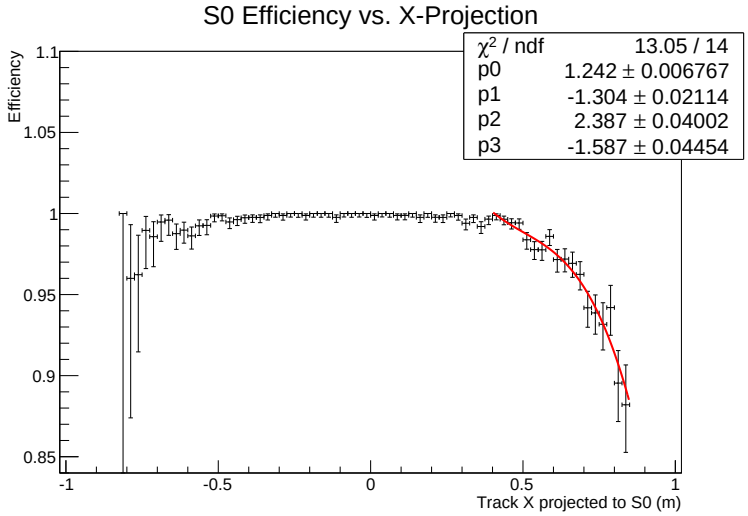

Figure 42: RHRS position-dependent S0 efficiency during the Fall 2016 run period. The horizontal axis shows the track projected to S0 in the spectrometer dispersive direction. The efficiency is parametrized using a 3^{rd} order polynomial fit from 0.4 meters $<$ X $<$ 0.85 meters; for X $<$ 0.4 meters, the efficiency is assumed to be constant.

C Stability Plots

We calculated the S0, S2m, and VDC 1-Track efficiencies separately for every run to make sure that the efficiencies did not change within a kinematic. We show the run-to-run stability for the S0, S2m, and VDC 1-Track efficiencies in figures 43, 44, and 45, respectively. No uncertainties are shown in the plots, but the observed run-to-run fluctuations are smaller than the statistical (binomial) uncertainties for each individual run.

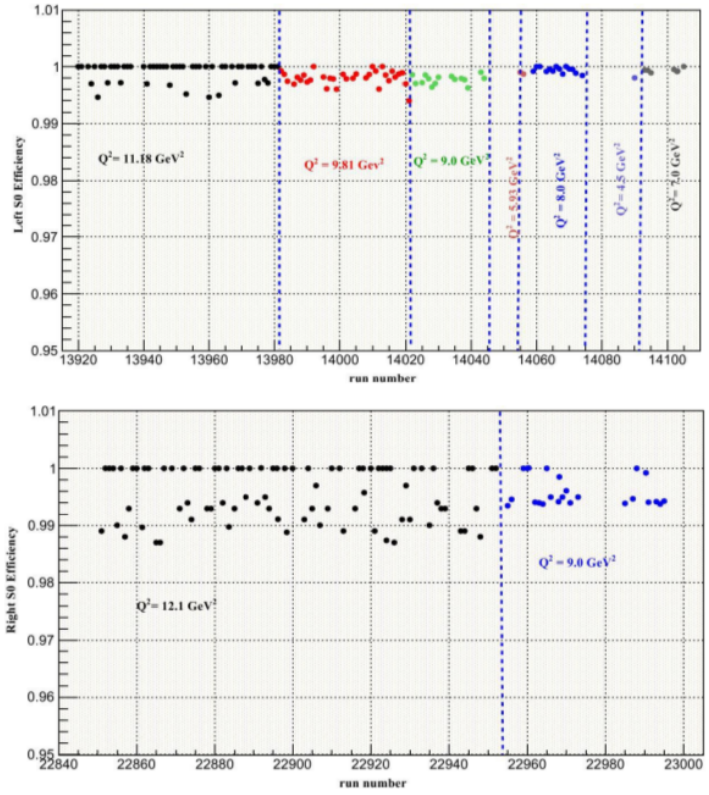

Figure 43: S0 Scintillator Efficiency Run-to-Run Stability.

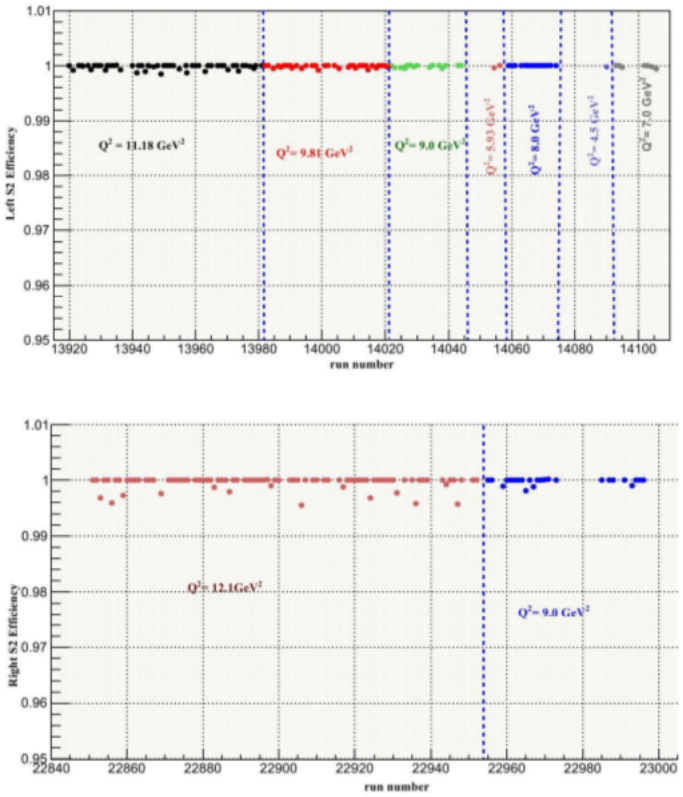

Figure 44: S2m Scintillator Efficiency Run-to-Run Stability.

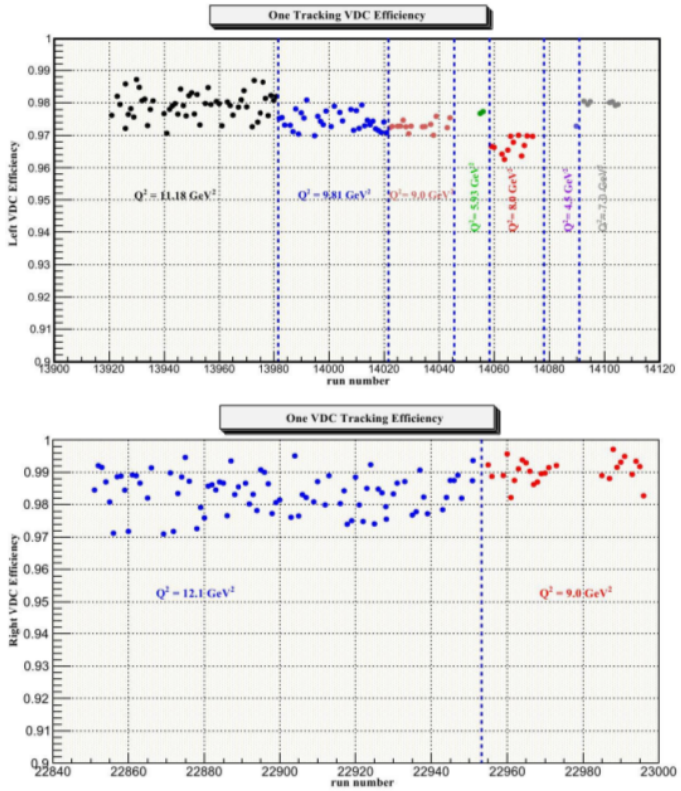

Figure 45: VDC 1-Track Efficiency Run-to-Run Stability.

References

[1] J. Arrington, S. Gilad, B. Moffit, and B. Wojtsekhowski *et al.*, *Jefferson Lab experiment E12-07-108 (GMp).*

[2] J. Alcorn *et al.*, *Nuclear Instruments and Methods A* **522** (2004) 294.

[3] V. Sulkosky, `Data Acquisition for the Hall A High Resolution Spectrometers During 12 GeV`.

[4] B. Schmookler, *Detector Position Determination*, `GMp Analysis Logbook Entry`.

[5] L. Ou, *Using Straw Chamber to Reconstruct Target Variables*, `GMp Analysis Logbook Entry`.

[6] J. Gomez *et al.*, *Phys. Rev. D* **49**, 4348 (1994).